The Astrophysical Journal, 852:94 (18pp), 2018 January 10 https://doi.org/10.3847/1538-4357/aa992c

GASP. VII. Signs of Gas Inflow onto a Lopsided Galaxy

Benedetta Vulcani[1,2], Bianca M. Poggianti[2], Alessia Moretti[2], Michela Mapelli[2], Giovanni Fasano[2], Jacopo Fritz[3], Yara Jaffé[4], Daniela Bettoni[2], Marco Gullieuszik[2], and Callum Bellhouse[4,5]
[1] School of Physics, University of Melbourne, VIC 3010, Australia
[2] INAF- Osservatorio Astronomico di Padova, Vicolo Osservatorio 5, I-35122 Padova, Italy
[3] Instituto de Radioastronomía y Astrofísica, UNAM, Campus Morelia, A.P. 3-72, C.P. 58089, Mexico
[4] European Southern Observatory, Alonso de Cordova 3107, Vitacura, Casilla 19001, Santiago de Chile, Chile
[5] University of Birmingham School of Physics and Astronomy, Edgbaston, Birmingham, England
Received 2017 June 9; revised 2017 October 15; accepted 2017 November 6; published 2018 January 11

Abstract

Theoretically, inflowing filaments of gas are one of the main causes of growth for a galaxy. Nonetheless, observationally, probing ongoing gas accretion is challenging. As part of the Gas Stripping Phenomena in galaxies with MUSE (GASP) program, we present the analysis of a spiral galaxy at $z = 0.04648$ whose characteristics indeed are consistent with a scenario in which gas accretion plays a major role. The most salient indirect parts of evidence that support this picture are as follows: (1) The galaxy is isolated, and its position rules out the mechanisms expected in dense environments. (2) It shows a pronounced lopsidedness extending toward the west. According to the spatially resolved star formation history, this component was formed $<6 \times 10^8$ years ago. (3) It has many large and elongated H II regions that are an indication of a fragmentation due to disk instability. (4) The stellar and gas kinematics are quite symmetric around the same axis, but in the gas the locus of negative velocities shows a convexity toward the east, as if new gas has been infalling with different orientation and velocity. (5) The metallicity distribution is inhomogeneous and shows exceptionally steep gradients from the center toward the outskirts, especially in the southwest side. (6) The luminosity-weighted age is generally low (∼8 Gyr) and particularly low (<7 Gyr) along a trail crossing the galaxy from southwest toward the north. It might trace the path of the accreted gas. These findings point to an inflow of gas probably proceeding from the southwest side of the galaxy.

Key words: galaxies: evolution – galaxies: general – galaxies: kinematics and dynamics – intergalactic medium

1. Introduction

A large fraction of galaxies in the local universe present a nonsymmetric light distribution in their disk, whose spatial extent is much larger along one half of the galaxy than the other (Baldwin et al. 1980; Block et al. 1994; Richter & Sancisi 1994; Rix & Zaritsky 1995; Schoenmakers et al. 1997; Zaritsky & Rix 1997; Haynes et al. 1998; Matthews et al. 1998; Swaters et al. 1999; Bournaud et al. 2005). The asymmetry is often visible also in the rotation curves, such that the shape and the maximum velocity are different in the two halves of a galaxy (e.g., Mihalas & Binney 1981; Jog 2002). The percentage of these galaxies depends on the environment: it is larger than 50% in Hickson compact groups (Rubin et al. 1991; Nishiura et al. 2000), and it is ∼25% in the field (Rubin et al. 1999; Zaritsky & Rix 1997; Sofue & Rubin 2001). Given the frequency of this phenomenon, the lopsided modes should be fairly long-lived (e.g., Baldwin et al. 1980) or excited frequently.

Generally, the lopsidedness is clearly visible in the gaseous component (H I) and occurs also in the central regions, where the nucleus is offset with respect to the outer isophotes. The asymmetry is of type $m = 1$, where m is the azimuthal wavenumber (e.g., Bournaud et al. 2005).

A similar fraction of galaxies (∼50%) also present deviations from the single plane and exhibit an integral shape with typical amplitudes of a few degrees in the stellar disk (e.g., Sanchez-Saavedra et al. 1990; Reshetnikov & Combes 1998; Ann & Park 2006). These galaxies usually also present even stronger warps in the neutral hydrogen (e.g., Sancisi 1976; Bosma 1981; Briggs 1990; Bottema 1995).

The asymmetry might be the result of different processes, such as tidal interactions (Beale & Davies 1969), mergers (Walker et al. 1996), satellite gas accretion (Zaritsky & Rix 1997), a lopsided dark matter halo (Jog 1997, 2002; Angiras et al. 2007), an off-center disk in the halo (Levine & Sparke 1998; Noordermeer et al. 2001), gas accretion (Bournaud et al. 2005), or, in clusters and groups, ram pressure stripping (e.g., Young et al. 2006). In addition to these externally triggered processes, the disk lopsidedness could also arise as a global instability in self-gravitating disks (Junqueira & Combes 1996; Bournaud et al. 2005). As discussed by Mapelli et al. (2008), the different scenarios might not be exclusive, and different processes could induce different degrees of lopsidedness in the different galaxy components. For example, ram pressure might create only moderate tidal gas tails in galaxies without inducing lopsidedness in the stellar population; galaxy interactions in the form of flybys might account for much stronger asymmetries simultaneously both in the gaseous and in the stellar disk; and gas accretion from filaments might produce even more pronounced lopsidedness, first in the gaseous disk, and only at later times in the stellar component, due to star formation in the asymmetric gaseous disk.

Several theoretical mechanisms have been proposed to explain the formation and maintenance of warped disks (e.g., Binney 1992; Kuijken & Garcia-Ruiz 2001; Sellwood 2013, and references therein). The proposed scenarios include discrete modes of bending in a self-gravitating disk (Toomre 1983; Sparke & Casertano 1988), misaligned dark halos (Dubinski & Kuijken 1995), galaxy interactions and

accretion of satellites (e.g., Huang & Carlberg 1997; Schwarzkopf & Dettmar 2001; Kim et al. 2014), direct accretion of intergalactic matter in the outskirts of galaxies (e.g., Revaz & Pfenniger 2001; van der Kruit 2007; Roškar et al. 2010), extragalactic magnetic fields (Battaner et al. 1990), and cosmic infall and outer gas accretion (e.g., Binney 1992). This large variety of proposed mechanisms and their modifications probably indicate that there is no single mechanism responsible for all observable warps in galaxies. The current situation looks like the largest warps are mostly caused by tidal distortions (Schwarzkopf & Dettmar 2001; Ann & Park 2006), whereas relatively small warps are triggered and supported by a variety of mechanisms.

Overall, the most promising processes to describe lopsidedness are tidal encounters and gas accretion, with the former being the dominant mechanism for group galaxies. Indeed, a perturbation due to a tidal encounter between two galaxies with an arbitrary orientation can generate a force term, which can then induce lopsidedness in the galaxy (Combes et al. 2004). Lopsidedness can also be generated more indirectly by the response of the disk to the distorted halo, which feels a stronger effect of the interaction (Weinberg 1995; Jog 1997; Schoenmakers et al. 1997). A generally stronger perturbation resulting from the infall of a satellite galaxy can also result in the disk lopsidedness, as shown in the *N*-body simulation study by Walker et al. (1996), who suggest that minor mergers can induce lopsidedness over a long timescale ($\sim$1 Gyr).

While tidal encounters can explain the observed amplitudes of disk lopsidedness, the *N*-body simulations by Bournaud et al. (2005) show that they cannot explain various observed statistical properties, such as the higher lopsidedness seen for the late-type field galaxies. Indeed, tidal encounters and mergers would tend to lead to the secular evolution of a galaxy toward earlier-type morphologies. Thus, if tidal interactions were the primary mechanism for generating lopsidedness, then the early-type galaxies should show a higher amplitude of lopsidedness. In addition, the amplitude of the lopsidedness seems not to correlate with the strength of a tidal encounter (Bournaud et al. 2005) or with the presence of nearby neighbors (Wilcots & Prescott 2004). Tidal encounters typically generate a fast mode that is not expected to be long-lived (Ideta 2002).

Thus mechanisms such as gas accretion from outside the galaxy need to be invoked to explain the lopsidedness in field galaxies.

There is growing evidence that galaxies steadily accrete gas from the external regions, as seen from cosmological models (Semelin & Combes 2005) and also as observed in nearby galaxies (Sancisi et al. 2008).

Smoothed particle hydrodynamics (SPH) simulations by Kereš et al. (2005) and grid-based adaptive mesh refinement simulations (e.g., Ocvirk et al. 2008) predict that galaxies can accrete large amounts of gas from the intergalactic medium (IGM) along cosmological filaments and show that a fraction of the inflowing gas is delivered to the disk not heated to the virial temperature of the halo (the so-called "cold accretion mode"; e.g., Kereš et al. 2005; Dekel & Birnboim 2006; Ocvirk et al. 2008; Brooks et al. 2009; Dekel et al. 2009; Faucher-Giguere 2011; Faucher-Giguère et al. 2011; van de Voort et al. 2011; Hobbs et al. 2015; Genel et al. 2012; Silk & Mamon 2012). The cold accretion mode appears to be most efficient at high redshifts ($z > 2$), but at low redshifts it seems to mainly occur in low-mass galaxies with $M_{\rm halo} \leqslant 5 \times 10^{11}\,M_{\odot}$.

However, more recently, Nelson et al. (2013) showed that the role of cold accretion might have been overestimated in previous smoothed particle hydrodynamics simulations. The new calculations, performed with the moving mesh code (AREPO, Springel 2010), indicate that the majority of gas is heated to the virial temperature before accreting onto the halo, at all galaxy masses (see also Torrey et al. 2012; Nelson et al. 2016).

The cold accreted gas does not necessarily mix with the existing gaseous halo, and over a few billion years it can represent a significant fraction of the disk mass itself (both as the gas phase and as newborn stars). This accretion can be asymmetrical (e.g., Jog & Combes 2009, and references therein), due to the different gas distributions along the filaments and to the different accretion rates.

The degree of lopsidedness decreases after a few gigayears, even if accretion is not stopped, because the disk reorients itself in regard to the filament. If there are more filaments with different accretion rates (e.g., Semelin & Combes 2005), the lopsidedness will generally be more moderate. In the simulations, when accretion is stopped, the lopsidedness has a typical lifetime of 3 Gyr (Bournaud et al. 2005).

Therefore, gas accretion can be the clue to explaining strong lopsidedness in galaxies that have no sign of recent interaction or merger.

Gas accretion might also induce the formation of clumps in the disk due to local gravitational instabilities. Clumping instabilities also cause starbursts, with a star formation rate typically enhanced by a factor of 10 in the present models. These bursts are thus not related to interactions, although the large-scale environment should influence this kind of activity indirectly through its role in the growth of disks (e.g., Elmegreen et al. 2007; Noeske et al. 2007).

Finally, another consequence of gas accretion might be metallicity gradients. This connection is poorly explored in the literature. Primordial gas accreted through filaments should be characterized by a lower metallicity than that of the target galaxy. Note that instead both flybys and ram pressure are expected not to significantly affect metallicity gradients (Mapelli et al. 2008). However, it is important to keep in mind that stars form from a mixture between the gas in the cold filament and the gas that was already in the disk. Moreover, if the gas accretion from the filament is not recent, but occurred in the past, phenomena like pollution from supernovae, stellar winds, and other feedback mechanisms might have already erased any metallicity gradient both in the gaseous and in the stellar component.

In the local universe, the advent of wide-field integral field spectroscopy (IFS) permits the study of metallicity gradients in a statistical way (e.g., Sánchez et al. 2014; Ho et al. 2015). Ongoing large IFS surveys include the Calar Alto Legacy Integral Field Area (CALIFA) Survey (Sánchez et al. 2012), the Sydney-AAO Multi-object Integral field spectrograph (SAMI) Survey (Croom et al. 2012), and the Mapping Nearby Galaxies at Apache Point Observatory (MaNGA) Survey (Bundy et al. 2015). Overall, disk galaxies have been found to universally exhibit negative metallicity gradients; that is, the center of a galaxy has a higher metallicity than the outskirts (e.g., Zaritsky

et al. 1994; Moustakas et al. 2010; Rupke et al. 2010; Sánchez et al. 2014, and references therein).

Gas accretion and metallicity gradients have also been studied at higher redshift. For example, Cresci et al. (2010) observed low-metallicity regions in three galaxies at $z \sim 3$, providing evidence for the actual presence of accretion of metal-poor gas in massive, high-z galaxies, capable of sustaining high star formation rates without frequent mergers of already evolved and enriched objects. In this paper, we present the analysis of an isolated spiral galaxy in the local universe presenting asymmetric features that we will argue are most likely due to cold gas accretion. This galaxy is drawn from GASP[6] (Gas Stripping Phenomena in galaxies with MUSE), an ongoing ESO Large program granted 120 hr of observing time with the integral field spectrograph MUSE mounted at the Very Large Telescope (VLT) aimed at characterizing where, how, and why gas can get removed from galaxies. A complete description of the survey strategy, data reduction, and analysis procedures is presented in Poggianti et al. (2017, Paper I). Briefly, GASP targets 94 "stripping-candidate galaxies" in a wide range of environments (from clusters to the general field) selected from a catalog built on a systematic search for galaxies with optical signatures of unilateral debris or tails. Such signatures are reminiscent of gas stripping processes or other processes leading to extraplanar star formation in outgoing gas (Poggianti et al. 2016). Targets are selected from WINGS (Fasano et al. 2006) and OMEGAWINGS (Gullieuszik et al. 2015) surveys and from the Padova Millennium Galaxy and Group Catalog (PM2GC; Calvi et al. 2011). Like all the other targets of GASP, the galaxy we discuss in this paper was selected for presenting a B-band morphological asymmetry suggestive of unilateral debris.

Throughout all the papers of the GASP series, we adopt a Chabrier (2003) initial mass function (IMF) in the mass range 0.1–100 $M_{\odot}$. The cosmological constants assumed are $\Omega_m = 0.3$, $\Omega_\Lambda = 0.7$, and $H_0 = 70$ km s^{-1} Mpc^{-1}. This gives a scale of 0.912 kpc/″ at the redshift of P11695, which is $z = 0.04648$.

2. The Target

The focus of this analysis is P11695 (R.A.: 10:46:14.78, decl.: +00:03:01.5), a galaxy at z = 0.04648 drawn from the Millennium Galaxy Catalog (Liske et al. 2003; Driver et al. 2005). Figure 1 shows a color composite image obtained by combining the reconstructed g, r, and i filters from the MUSE data cube. It appears evident that P11695 is an asymmetric spiral galaxy possessing trails of bright knots across the disk. The galaxy seems also to be characterized by a small U-shaped warp.

2.1. Observations

Following the GASP strategy, P11695 was observed in service mode with the MUSE spectrograph, mounted at the Nasmyth focus of the UT4 VLT, at Cerro Paranal in Chile. It was observed on 2016 January 9 and 10, with photometric conditions; the seeing at 650 nm (measured on the telescope guide star) remained below 0.″7 during the whole observing block. A total of four 675 s exposures were taken with the Wide Field Mode.

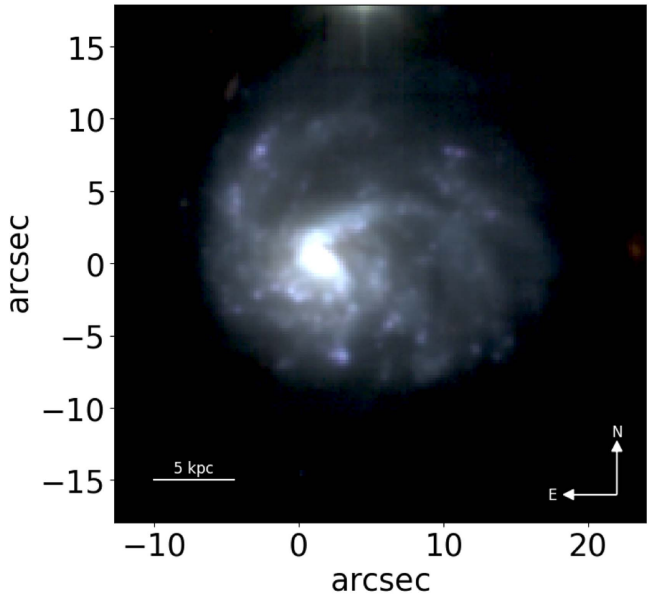

Figure 1. RGB image of P11695. The reconstructed g, r, and i filters from the MUSE cube have been used. At the galaxy redshift, 1″ = 0.912 kpc; see scale. North is up, and east is left.

MUSE is composed of 24 IFU modules, and each of them is equipped with a $4k \times 4k$ CCD. The spectral coverage spans the wavelength range between 4500 Å and 9300 Å, with a sampling of 1.25 Å/pixel and a spectral resolution of ∼2.6 Å. The 1′ × 1′ field of view is sampled at ∼0.″2/pixel; each data cube therefore consists of $\sim 10^5$ spectra.

2.2. Data Reduction

The data reduction process for all galaxies in the GASP survey is presented in Paper I. Briefly, raw data were reduced using the latest ESO MUSE pipeline available at the time of observations (v1.2.1).

As the data have sufficient sky coverage, the sky was modeled directly and subtracted from individual frames using the 20% of pixels with the lowest counts. After wavelength calibration using arc lamp exposures, the final wavelength adjustments were made using sky emission lines. The final, flux-calibrated data cube was generated by lining up and combining the individual frames using sources in the white-light images and consists of 329 × 329 spectra with radial velocities corrected to the barycenter of the solar system. The FWHM of point-like sources on the image obtained by convolving the final MUSE data cube with the V-band filter is 0.″8 (four pixels).

3. Analysis

Figure 2 shows the white-light image from MUSE (4750–9350 Å). From now on, we will use the contours representing the distribution of the oldest stellar population (see Section 3.6 and Figure 14) to define the "original body" of the galaxy. Instead, we will call the "main body" of the galaxy the region containing the spaxels whose near-Hα continuum flux is $\sim 1\sigma$ above the background level (see also Paper I).

[6] http://web.oapd.inaf.it/gasp/index.html

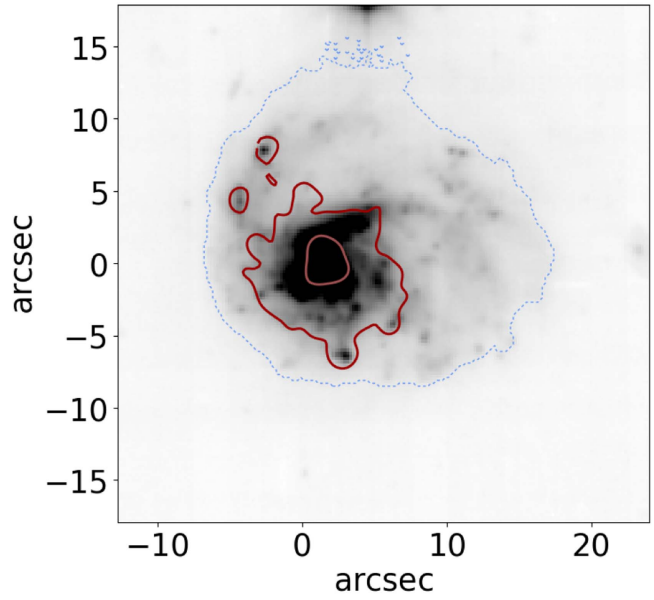

Figure 2. MUSE white-light image of P11695. Red solid contours are the distribution of the oldest stellar population (see Figure 14), which from now on we call the "original body." The light blue dashed contour shows the "main body."

The lopsided shape of the galaxy clearly stands out. Traces of debris to the north and west of the main body and bright knots distributed across the galaxy appear evident.

The presence of the knots becomes even more striking in the MUSE Hα map, shown in Figure 3. The standard procedure developed within the GASP project to identify these Hα knots (see Paper I for details) detected 101 knots, less than 10 of which are outside the main body. However, this automatic procedure assumes all of the knots have a round shape, but, as is evident from Figure 3, this is not the case for P11695. We therefore developed another procedure that selects all of the regions with a $\log(\mathrm{H}\alpha[\mathrm{erg/s/cm^2/arcesc^2}])$ flux larger than (the arbitrary value of) -16.2. Many other fainter knots are visible, but, to be conservative, we choose to focus only on the brightest ones. The right panel of Figure 3 shows the 29 bright knots we detected with this approach. We note that while many other stripping candidates in the GASP sample are characterized by a conspicuous number of knots, usually these are located mainly in the stripping tails and have a round shape (Paper I; Gullieuszik et al. 2017; Paper IV). In contrast, almost all of the knots in P11695 are located on the galaxy disk, and they clearly show elongated shapes. These peculiarities induce us to pay particular attention to the properties of the knots, and in what follows we will characterize them separately.

In the left panel of Figure 3 we overplot the contours of the original body to the Hα flux map. The latter is much more extended than the older stellar population, especially on the west side of the galaxy, showing how the galaxy grew in size over time.

3.1. Dust

The Hα fluxes presented in Figure 3 were corrected for extinction by dust internal to P11695. The map of the dust extinction A_V is obtained from the absorption-corrected Balmer decrement in each spaxel. As described in Paper I, we assumed an intrinsic Hα/Hβ ratio equal to 2.86 and adopt the Cardelli et al. (1989) extinction law. The A_V map has been calculated only for spaxels where the signal-to-noise ratio (S/N) on the Hα and Hβ lines is larger than 3 and the ratio of the two lines is larger than the assumed 2.86 value for the Balmer decrement.

The A_V map (Figure 4) shows that, overall, P11695 is characterized by low values of extinction, almost always <1 mag. The northwest side of the galaxy has a systematically larger extinction than the southeast side. Note, however, that the in the east side of the galaxy there are many regions where A_V is not measured. In these regions indeed Hβ might be undetected because of obscuration by dust.

To compute the dust extinction of the Hα knots, we assign the median value within each knot to all the spaxels in that knot, so spaxels with no measurement in the left panel of Figure 4 might have an associated measurement in the right panel. The A_V estimate in the knots can be therefore considered as a lower limit of the true values. However, we have compared these values to those obtained by integrating over the spectra in each knot, finding good agreement. We find that not all of the knots are highly extincted, as we would expect in strongly star-forming regions. Overall, there does not seem to be a strong correlation between the position of the knots and the distribution of the dust.

3.2. Gas Ionization Mechanism

The next step is to characterize the ionizing sources as a function of the position and detect the possible presence of an active galactic nucleus (AGN). We therefore inspect the diagnostic diagrams (e.g., Kewley et al. 2006) based on the emission lines located within our cube observed range (i.e., Hβ, [O III] 5007 Å, [OI] 6300 Å, Hα, [N II] 6583 Å, and [S II] 6716 +6731 Å). The lines' intensities were measured after subtraction of the continuum, exploiting the pure stellar emission best-fit model provided by our spectral fitting code SINOPSIS (Fritz et al. 2017, Paper III, see Section 3.6), to take into account any possible contamination from stellar photospheric absorption. Only spaxels with an $S/N > 3$ in all of the emission lines involved were considered.

All of the diagnostic tools are concordant that the emission-line ratios are consistent with gas being photoionized by young stars ("star-forming" according to Kauffmann et al. 2003; Kewley et al. 2006). As an example, Figure 5 shows [O III] 5007/Hβ versus [N II]6583/Hα.

Véron-Cetty & Véron (2003) classified P11695 (identified as SDSS J10462+0003) as Seyfert 1, but this catalog is obsoleted by Véron-Cetty & Véron (2006), which does not detect any sign of AGN activity, in agreement with our results.

We also characterize the main source of ionization for the Hα knots, and, according to BPT diagrams, they are all powered by star formation (plot not shown).

3.3. Integrated and Spatially Resolved Star Formation Rate

Having assessed that the ionization source in P11695 is mostly photoionization by young stars, we can now measure the total ongoing star formation rate (SFR), obtained from the dust- and absorption-corrected Hα luminosity by adopting the Kennicutt (1998) relation for a Chabrier (2003) IMF: $\mathrm{SFR} = 4.6 \times 10^{-42}\, \mathrm{L_{H\alpha}}$. Integrating the spectrum over the galaxy main body, for the spaxels with an S/N (Hα) > 3, we get a value of SFR $= 3.27\ M_\odot\ \mathrm{yr}^{-1}$. The total SFR in the H$\alpha$ knots is $1.70\ M_\odot \mathrm{yr}^{-1}$: half of the current SFR is therefore taking place in these H II regions. This value can be considered

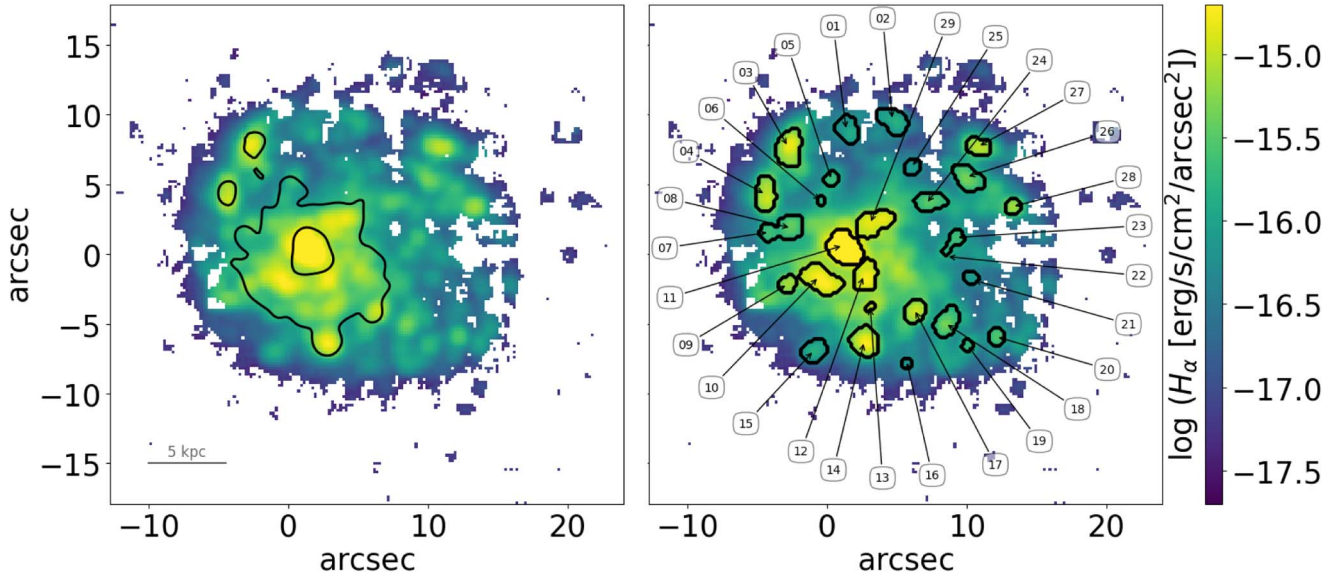

Figure 3. MUSE map (median filtered 5 × 5 pixels) for Hα S/N > 4, uncorrected for stellar absorption and intrinsic dust extinction, but corrected for Galactic extinction. Left: Contours represent the original body (see Figure 14). Right: Contours identify 29 bright Hα knots, which are also identified by a number (see text for details).

a lower limit to the total SFR in the knots; indeed, the contribution of the Hα flux escaped from the knots is not taken into account.

Figure 6 shows the spatial distribution of the SFR in the Hα knots. The SFR in all of the spaxels included in each knot is summed up. The central knot has a very high value of SFR, while all the other regions are producing stars at a much lower rate (<1: 3).

3.4. Stellar and Gas Kinematics

We now characterize separately the kinematics of the gas and stellar components (Figure 7).

The kinematic properties of the gas were inferred by the analysis of the characteristics of emission lines, especially Hα, by exploiting the KUBEVIZ (Fossati et al. 2016) code. In the MUSE wavelength range, the typical spectral dispersion of 1.25 Å pixel^{-1} translates to a velocity scale of 25 km s^{-1} pixel^{-1}. The average FWHM resolution is 2.51 Å, equivalent to 110 km s^{-1}. Details on the methods can be found in Paper I.

The stellar kinematic was instead derived from the analysis of the characteristics of absorption lines, using the pPXF software (Cappellari & Emsellem 2004), which works in Voronoi binned regions of given S/N (15 in this case; see Cappellari & Copin 2003). The value of the stellar radial velocity was further smoothed using the two-dimensional local regression techniques (LOESS) as implemented in the Python code developed by M. Cappellari.[7]

The velocity fields of the two components are corotating around the same axis, approximately the north–south direction (slit B in Figure 7), and span a similar velocity range ($-90 < v(\mathrm{km\ s^{-1}}) < 90$).[8] In both cases, the west side is characterized by negative velocities, indicating that that side is approaching. The gas uncertainties in most of the spaxels are <2.5 km s^{-1}, except in the very external regions. Uncertainties on the stellar motion are the formal errors of the fit calculated using the original noise spectrum data cube and have been normalized by the χ^2 of the fit. These errors are systematically larger (∼20–30 km s^{-1}) than those for the gas, reflecting the quality of the fit, but are still much smaller than the measured velocities, reassuring us about the robustness of our results.

In the gas, the locus of negative velocities shows a bending in the external regions, with the convexity pointing toward the east.

The velocity dispersion maps highlight some differences between the two components. In the original body, the $\sigma_{\rm gas}$ goes from ∼15 to 50 km s^{-1}, while $\sigma_{\rm stars}$ ranges from 50 to ∼75 km s^{-1} and does not increase toward the center. In the outskirts, the velocity dispersion of the gas is always relatively low (∼10–20 km s^{-1}), indicative of a dynamically cold medium, except on the south and east edges of the galaxy, but there the low S/N ratio of these spaxels prevents us from drawing solid conclusions. In contrast, the motion of the stars is much more random, as indicated by the stellar σ that reaches peaks of $\sigma > 250$ km s^{-1} in the northern regions. Nominal errors on the dispersions are similar to uncertainties on the velocities, both for the gas and the stars.

To better contrast the gas and stellar kinematics, we extract the velocity profiles (Figure 8) along the rotation axis and its perpendicular direction (B and A in Figure 7, respectively). We deproject the radius considering the position angle and inclination (the inferred position angle is 40°, and the inferred inclination is 42°). We compute the average value of the spaxels entering the slit at each distance, weighted for the corresponding errors. Along slit A, the gas presents a quite regular rotation. In the central part of the galaxy (±3″), the variation of the velocity is quite steep, and then it flattens out and the curves are almost flat. The stars follow the same trend, even though the curve is more noisy. In contrast, along slit B, for both components the curve is always quite flat, even though with many local variations. This was expected since slit A is approximately 90° from the rotation axis.

[7] http://www-astro.physics.ox.ac.uk/~mxc/software

[8] We applied a shift in velocity of 25 km s^{-1} to the gas to force the velocities of the two components to be the same in the galaxy center.

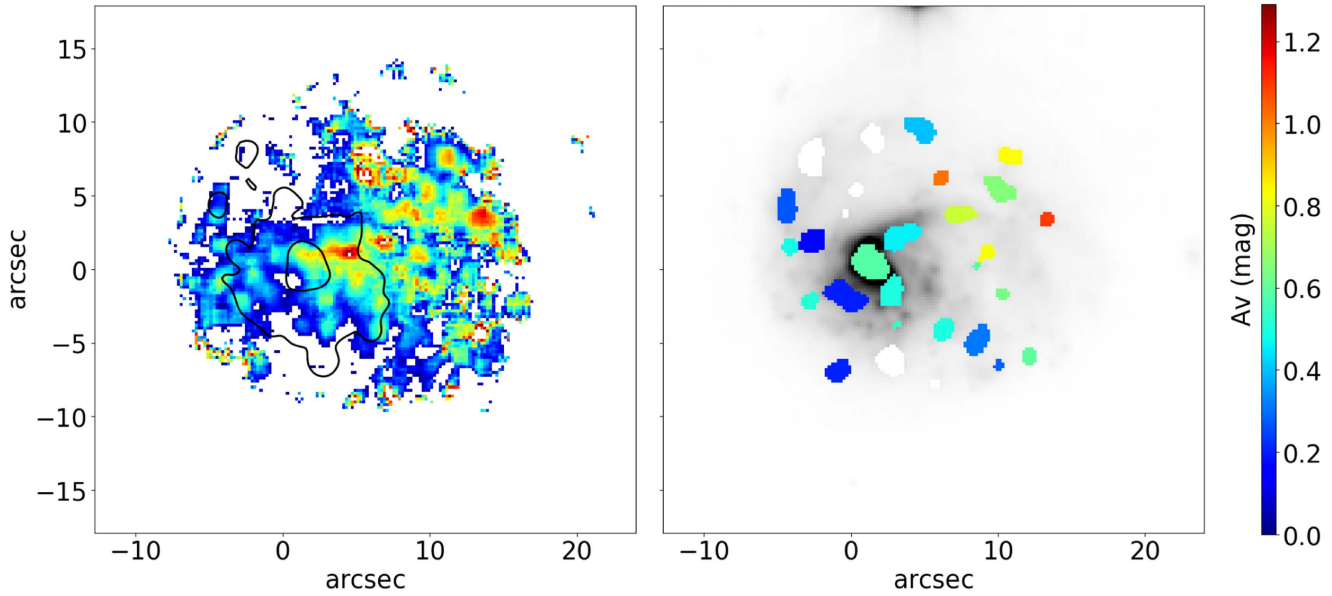

Figure 4. A_V map. Only spaxels with an S/N (Hα) > 3 are shown. Left: Contours represent the original body (see Figure 14). Right: Only regions corresponding to the 29 Hα knots identified in Figure 3 are color coded according to the median A_V of each knot. Hα knots with >50% of the spaxels without determination of the Hβ are colored in white. In the background, the white-light image of the galaxy (Figure 2) is shown, for reference.

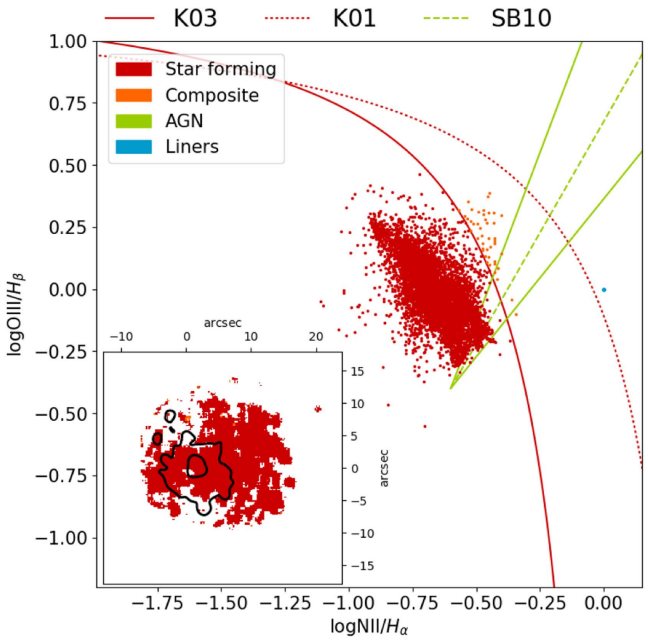

Figure 5. Diagnostic diagram for [O III]5007/Hβ vs. [N II]6583/Hα. Lines are from Kauffmann et al. (2003, K03), Kewley et al. (2001, K01), and Sharp & Bland-Hawthorn (2010, SB10) to separate star-forming, composite, AGN, and LINERS. In the inset, the BPT line-ratio map is shown. Only spaxels with an $S/N > 3$ in all of the emission lines involved are shown.

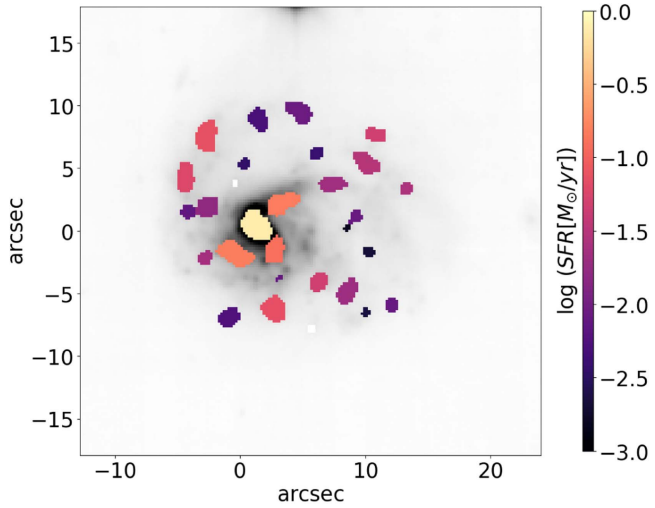

Figure 6. Total SFR produced in each of the 29 Hα knots identified in Figure 3. In the background, the white-light image of the galaxy (Figure 2) is shown for reference.

3.5. Spatially Resolved Gas Properties

The gas metallicity and ionization parameter for each star-forming spaxel were calculated using the pyqz Python module7 (Dopita et al. 2013) v0.8.2; the $12 + \log(O/H)$ and $\log(q)$ values are obtained by interpolating from a finite set of diagnostic line-ratio grids computed with the MAPPINGS code. We used a modified version of the code (F. Vogt 2017, private communication) to implement the MAPPING IV grids that are calibrated in the range $7.39 < 12 + \log(O/H) < 9.39$, which is broader than the metallicity range covered by MAPPING V grids. Our results are based on the [N II]6585/[S II]6717+6731 versus [O III]/[S II] 6717+6731 (see Paper I). As discussed in detail by Kewley & Ellison (2008), the systematic errors introduced by modeling inaccuracies are usually estimated to be ~0.1–0.15 dex, whereas discrepancies of up to 0.2 dex exist among the various calibrations based on photoionization models.

The ionization parameter is quantified as the ionizing photon flux through a unit area divided by the local number density of hydrogen atoms. The spatial distribution of the ionization parameter for P11695 is presented in Figure 9. It is generally very low, in the range $6.5 < \log(q) < 7$. This is in agreement with other galaxies in the GASP survey (Paper I, Paper IV), even though in this case a clear clumpy pattern emerges, while in other galaxies a more smooth distribution is observed. Hα knots tend to have a systematically large value of q: the median value integrated across the entire galaxy is 6.5, while the median value in the Hα knots is 6.7.

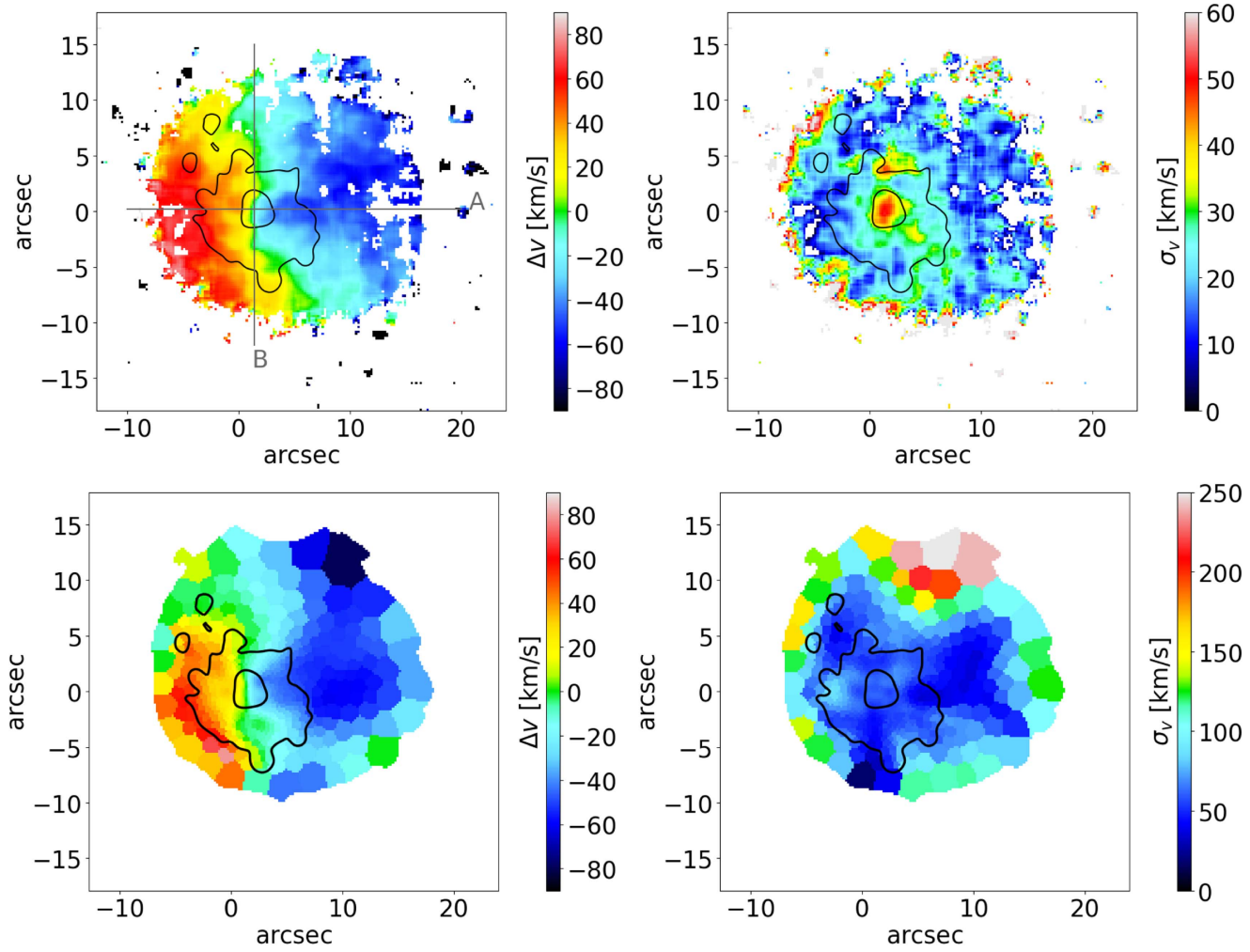

Figure 7. Top: Hα velocity (left) and velocity dispersion (right) map for 5 × 5 spaxels with S/N Hα > 4. Bottom: stellar velocity (left) and velocity dispersion (right) map for Voronoi bins with S/N > 15. Contours represent the original body (see Figure 14). In the Hα velocity map, the axis along which profiles are extracted are shown (A and B).

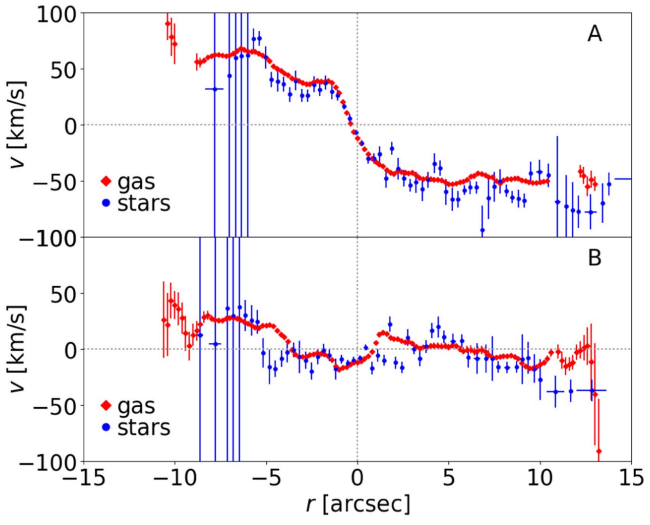

Figure 8. Velocity profiles along the two slits shown in Figure 7 (A, B), as indicated in the labels, both for the gas and the stars. Distances are deprojected considering the galaxy inclination and position angle. Values and vertical errors are weighted by the formal errors; for the stellar velocity, horizontal errors indicate the width of the Voronoi bins.

Figure 10 shows that the spatially resolved metallicity is overall quite low, in the range $7.4 < 12 + \log(O/H) < 8.5$, with an average value of 8.04. The maximum of the metallicity corresponds to the maximum of the Hα flux. According to the Tremonti et al. (2004) mass–metallicity relation, a galaxy with mass similar to that of P11695 should have a metallicity of $12 + \log(O/H) \sim 8.99$. However, the uncertainties in the absolute calibration of the metallicity scale (F. Vogt 2017, private communication) prevent us from drawing solid conclusions regarding the low metallicity of P11695.

The galaxy shows a sharp decrease in its metallicity from the center toward the outskirts. The metallicity distribution is inhomogeneous, and it is not characterized by spherical symmetry. For example, two regions of very low metallicity stand out in the southwest and northeast sides of the galaxy, while the northwest side has systematically higher metallicity values.

The metallicity in the Hα knots (right panel of Figure 10) follows the trend of the entire galaxy: those in the center are more metal-rich, and those in the outskirts have lower values of metallicity, especially on the southwest and north sides of the galaxy.

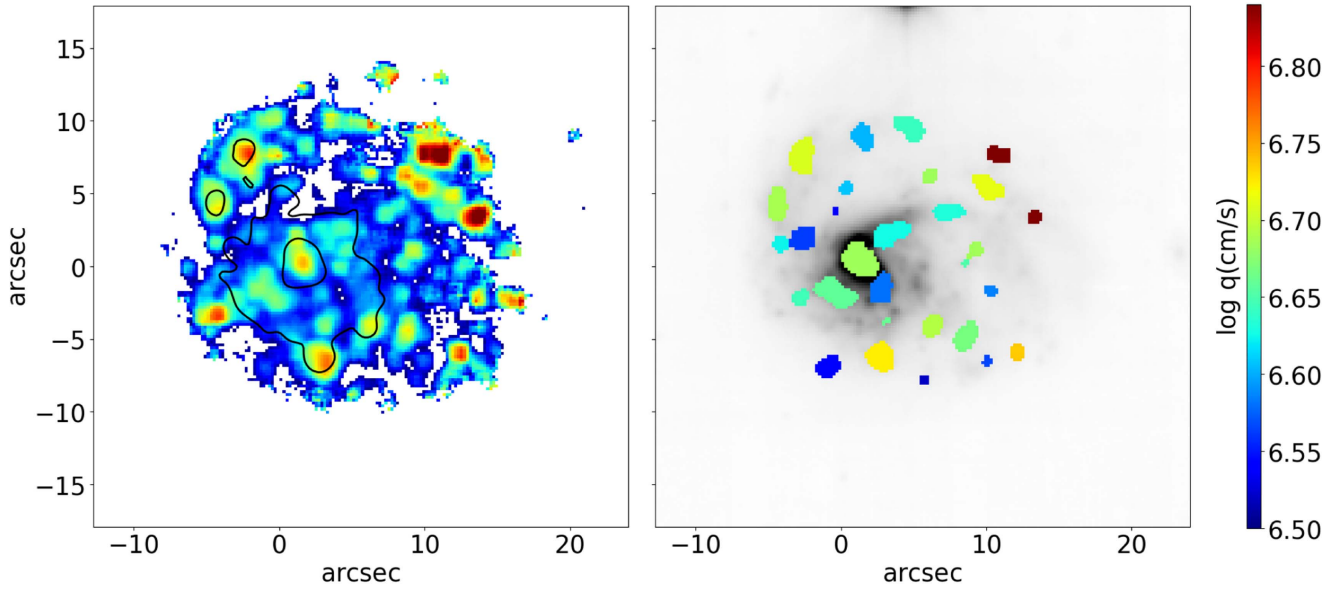

Figure 9. Ionization parameter (q) map. Left: Contours represent the original body (see Figure 14). Right: Only regions corresponding to the 29 Hα knots identified in Figure 3 are color coded according to the median q of each knot. In the background, the white-light image of the galaxy (Figure 2) is shown for reference.

Trends between metallicity and distance from the galaxy center are more clear in Figure 11, where metallicity gradients along different axes are shown. To start, we use the axis defined by the velocity maps (slits A and B in Figures 7 and 10). In order to get more signal in the galaxy outskirts, instead of extracting gradients along a slit, we select all of the spaxels within conic apertures $\pm 3^{\circ}$ wide around the slits and take the median of the metallicity as a function of distance. This choice also allows us to compute errors as the standard deviation within the aperture. Along A, the gradients extracted on the two sides (east negative and west positive) of the galaxy are quite similar, except that on the west side at $1'' < |r| < 2''$ there is a steeper decline in the metallicity values with distance than on the other side. Trends are inverted at $|r| \sim 4''$, where the east side is more metal-poor than the west side. Along B, gradients are symmetric around the 0 position up to $5''$; then the north side of the galaxy presents a systematically higher metallicity.

Clearly, these two axes do not capture the largest variation of metallicity in the galaxy. We therefore use three additional axes (C, D, E), which are chosen ad hoc to better characterize the variations across the galaxy. The chosen apertures are shown in the left panel of Figure 10 and are 30°, 20°, and 20° wide, respectively. While gradients along D are similar to those along B, the panels in the third row of Figure 11 show that the gradients along C are the steepest ones. The minimum metallicity is $\log(\mathrm{O/H}) \sim 7.7$, while along A and B, for example, it is always >7.9. Finally, the E aperture catches one of the flattest gradients in the galaxy, with metallicity values >8 at all distances.

To understand if these results are in some sense peculiar or are similar to those of other galaxies in the local universe, in the right panels of Figure 11 we compare the metallicity gradients of P11695 to those tabulated by Pilyugin et al. (2014), who investigated the oxygen abundance distributions across the optical disks of 130 nearby late-type galaxies, and by Ho et al. (2015), who measured the average metallicity of ~50 nearby galaxies mainly drawn from the CALIFA (Sánchez et al. 2012) survey. For all of the samples, r_{25} has been computed as the major axis of the isophote of surface brightness = 25 in the B band, and radii are deprojected considering the position angle and inclination. As P11695 has a very lopsided optical light distribution, a single scale length might not be representative of the entire galaxy. Therefore, we also compute r_{25} considering separately the west side and the east side of the galaxy. In the right panels of Figure 11, while the profiles represented by the symbols are scaled using the average scale length $r_{25} = 16.''25$, profiles shown in shaded areas are scaled using the most appropriate scale length: the positive sides of the profiles extracted along A, C, D, and E are scaled using $r_{25} = 18.''57$, and the corresponding negative sides are scaled using $r_{25} = 13.''93$. For the profiles along slit B, the average scale length is adopted. As expected, the slope of the profiles depends on the adopted scale length, but the general conclusions hold. To renormalize the Pilyugin et al. and Ho et al. samples to ours, we assume that the maximum central metallicity coincides in all of the samples. This normalization allows us to compare the gradients regardless of the uncertainties related to the absolute calibrations adopted by the different works. Overall, P11695 presents the steepest gradients. Differences are the largest for the trends extracted along the aperture C and the smallest for trends extracted along E. P11695 is therefore at the tail of the metallicity–radius distribution.

3.6. Integrated and Spatially Resolved Stellar Population Properties

The spectral fitting code SINOPSIS (Paper III) allows us to characterize the spatially resolved properties of the stellar populations. Details can be found in Paper I and Paper III. Briefly, this code combines different simple stellar population spectra to reproduce the observed equivalent widths of the main absorption and emission lines and the continuum in various bands. The main outputs of SINOPSIS are maps of stellar mass, average star formation rate, and total mass formed in four age bins, for luminosity-weighted and mass-weighted stellar ages. In addition, it also produces a best-fit model data cube for the stellar-only component.

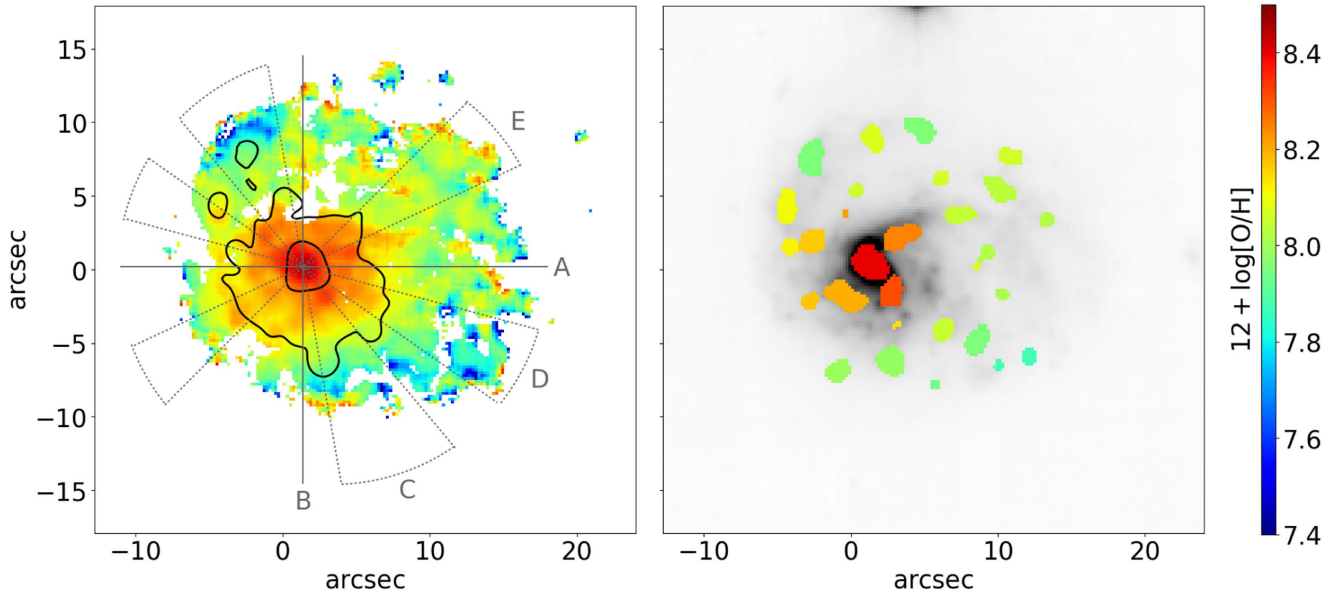

Figure 10. Metallicity map. Left: contours represent the original body (see Figure 14). Slits (A), (B) and conic apertures (C)–(E) used to extract metallicity gradients are also shown. Right: only regions corresponding to the 29 Hα knots identified in Figure 3 are color coded according to the median metallicity of the knots. In the background, the white-light image of the galaxy (Figure 2) is shown for reference.

Running SINOPSIS on the galaxy integrated spectrum obtained within the galaxy main body, we find the total stellar mass measured is $M_* = 1.17 \times 10^{10} M_\odot$. Considering the total SFR measured in Section 3.3, P11695 lies on the upper envelope of the typical SFR–mass relation for star-forming field galaxies (see Poggianti et al. 2016).

Figure 12 presents the map of the luminosity-weighted age. This provides an estimate of the average age of the stars weighted by the light we actually observe, therefore giving us an indication of when the last episode of star formation occurred. The map shows that the typical luminosity-weighted age of the galaxy is $\sim 10^{8-8.5}$ years. The distribution of ages is quite homogeneous, except in some regions, where the stars are much younger ($\sim 10^{6.5}$ years). In most of the cases, these regions coincide with the Hα knots, even though there are some knots with older ages and some young regions not included in any knot (see the trail in the southern part of the galaxy). Overall, the knots have an age typically less than $10^{7.5}$ years. The youngest knots are located in the southwest side of the galaxy, and two very young ($\sim 10^{6.5}$ years) knots are located on the opposite side and others on the northwest side.

Comparing the luminosity-weighted age and the ionization parameter (Figure 13), we find a clear anticorrelation, both for the spaxels in the Hα knots and for those outside. This trend suggests that we might be able to infer the level of ionization in a galaxy given the age of its stellar population, or vice versa. Within the GASP sample, other galaxies present very different correlations. Understanding the physical meaning of this result is beyond the scope of this work and will be investigated in a subsequent paper.

Finally, we can investigate how the SFR varied with cosmic time. We choose four logarithmically spaced age bins in such a way that the differences between the spectral characteristics of the stellar populations are maximal (Fritz et al. 2007 and Paper III).

The bottom right panel of Figure 14 shows the SFR that took place in the oldest age bin ($t > 5.7 \times 10^9$ years). This is the bin we use to define the contours indicating the original body shown in all of the previous figures. During this epoch, the SFR is high only within the original body, which assembled over this time. Very little SFR is found far from the galaxy core ($\sim 10''$). At this stage, the galaxy does not show any sign of asymmetry. In the following age bin (5.7×10^8 years $< t < 5.7 \times 10^9$ years), the galaxy SFR is still mainly concentrated in the original body, and the SFR in the outer region is still low. In the next age bin (2×10^7 years $< t < 5.7 \times 10^8$ years), the SFR in the galaxy is boosted and the galaxy develops, especially toward the west side. This is the epoch when the total SFR is the highest and the galaxy has the largest extension. The map is not smooth, suggesting the SFR is taking place in a nonuniform way. Finally, in the current SFR ($t < 2 \times 10^7$ years), the core of the galaxy is still highly star-forming, while in the external regions a decline in the SFR is observed. A conspicuous number of highly star-forming regions are visible. Overall, they correspond to the knots seen in the Hα maps.

The star formation history (SFH), that is, the average SFR in the four age bins, computed by summing the SFR in the spaxels divided by the number of spaxels, is presented in Figure 15 as black lines, for both the region within and outside the original body. The trends just discussed emerge clearly: the original body developed in the earlier epochs, and the galaxy was forming stars at a quite high rate already in the second-oldest age bin, while the external part developed in a later phase, and a strong SFR increase happened only during the last 5.7×10^8 years. Both regions peak within 2×10^7 years $< t < 5.7 \times 10^8$ years ago. The same figure also shows the SFHs of each Hα knot separately. The SFHs of the Hα knots within and outside the original body follow the trends of all the spaxels in the same regions, respectively, with some exceptions. Among the Hα knots with rising SFR, 13, 14, and 17 (within the original body) and 16, 18, and 19 (outside) are all located in the southwest side of the galaxy. Hα knots 3 and 4 are instead in the opposite side, in the northeast side. Finally, Hα knots 26,

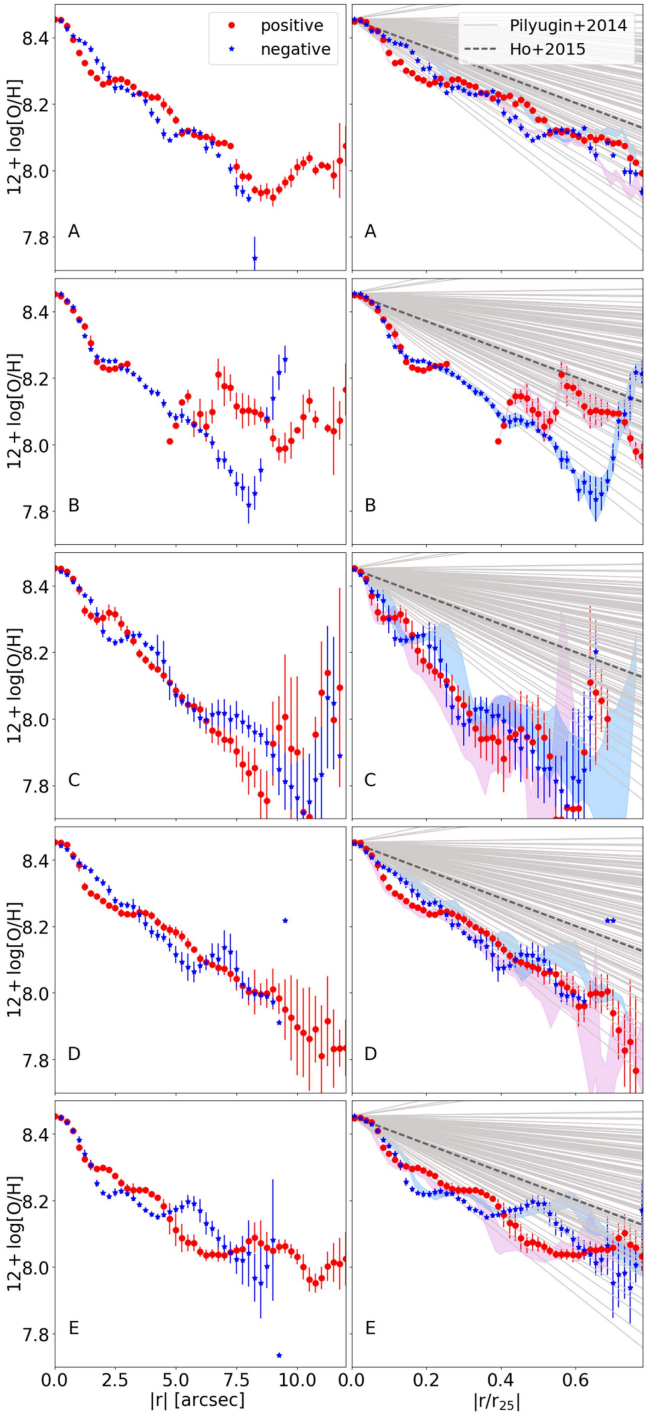

Figure 11. Metallicity gradients extracted along the directions (A)–(E) shown in Figure 10. Errors represent the standard deviation (σ) computed using the values falling into the apertures. Red points correspond to the side of the slits north or west of the center (positive arcsecs); blue points correspond to the side of the slits south or east of the center (negative arcsecs). Left: profiles in arcsec, not deprojected. Right: profiles normalized by a scale radius; all distances are deprojected considering the galaxy inclination and position angle. Shaded areas represent the profiles normalized by adopting different scale lengths (see text for details). Gray lines are from Pilyugin et al. (2014) and Ho et al. (2015).

27, and 28 are on the western side, in the outskirts. The last four seem to be located on the extension of the same spiral arm.

This analysis shows how Hα knots located at similar distances from the center but in different regions of the galaxy have a quite different history, suggesting they were born in different conditions.

4. Discussion

In this section, we aim to draw a scenario for the formation and evolution of P11695 that is able to explain its main characteristics illustrated in the previous sections. First, we need to characterize the environment around the galaxy, in order to shed light on the possible physical mechanisms acting on it.

4.1. The Environment

P11695 does not belong to any recognizable cluster or group: it has been selected as isolated from both our own environmental catalog (Calvi et al. 2011) and an independent catalog assembled by Argudo-Fernández et al. (2015). Paccagnella (2018) estimate that it is embedded in a halo of mass $M_* = 3.9 \times 10^{11}\,M_\odot$.

Figure 16 shows the spatial distribution of all galaxies around P11695 with measured redshift in the range $0.025 < z < 0.07$. Redshifts are taken from the MGCz (Driver et al. 2005) and SDSS-DR9 (Ahn et al. 2012). The estimated spectroscopic completeness in this region of the sky is >96% at B = 20 (Liske et al. 2003; Driver et al. 2005). In agreement with Argudo-Fernández et al. (2015), the closest galaxy at the same redshift is at 2.3 Mpc. Calvi et al. (2011) and Tempel et al. (2012) identified overall three groups in this area, whose positions are highlighted in Figure 16 and whose properties are listed in Table 1. The spectroscopic galaxy sample adopted by Tempel et al. (2012) to identify the groups is complete up to the Petrosian magnitude $m_r = 17.77$ (Strauss et al. 2002).

Their redshift difference with respect to P11695 corresponds to a relative velocity of ~2000 km s^{-1}. This difference in velocity is >~10× the velocity dispersion of the largest group. Therefore, if P11695 ever belonged to one of these groups, it should now move at an unrealistic velocity. We therefore tend to exclude that the galaxy was formed in one of the groups and was subsequently kicked out of it.

To firmly exclude the presence of massive structures around P11695, we searched for X-ray emission within 30″ from the galaxy. *ROSAT* (0.1–2.4 keV) and SWIFT (15–25 keV, 25–45 keV, 50–194 keV) data are available in this region of the sky, and both failed to detect any extended structure, which could be connected to the presence of a group or cluster.

P11695 is therefore a truly isolated galaxy, and the typical mechanisms usually invoked to explain the observed tails, such as ram pressure stripping due to the interaction between the hot and dense intragroup/cluster medium and the galaxy gas (Gunn & Gott 1972) or tidal interactions (Byrd & Valtonen 1990), have to be ruled out, because they generally take place in more massive or at least richer environments.

In addition, no clear sign of recent merger is visible in any part of the analysis we have conducted, and there is no visible companion. Note that even if we do not observe companions now, they might have merged with P11695 in the past. Walker et al. (1996) show that perturbations induced by a minor merger can last for 1 Gyr. However, it is not clear whether a minor merger can induce significant lopsidedness for a sufficiently long time. Walker et al. (1996) show that minor mergers can substantially heat and puff up the disk, driving the formation of a strong bar ($m = 2$ mode). Their simulated galaxies are not

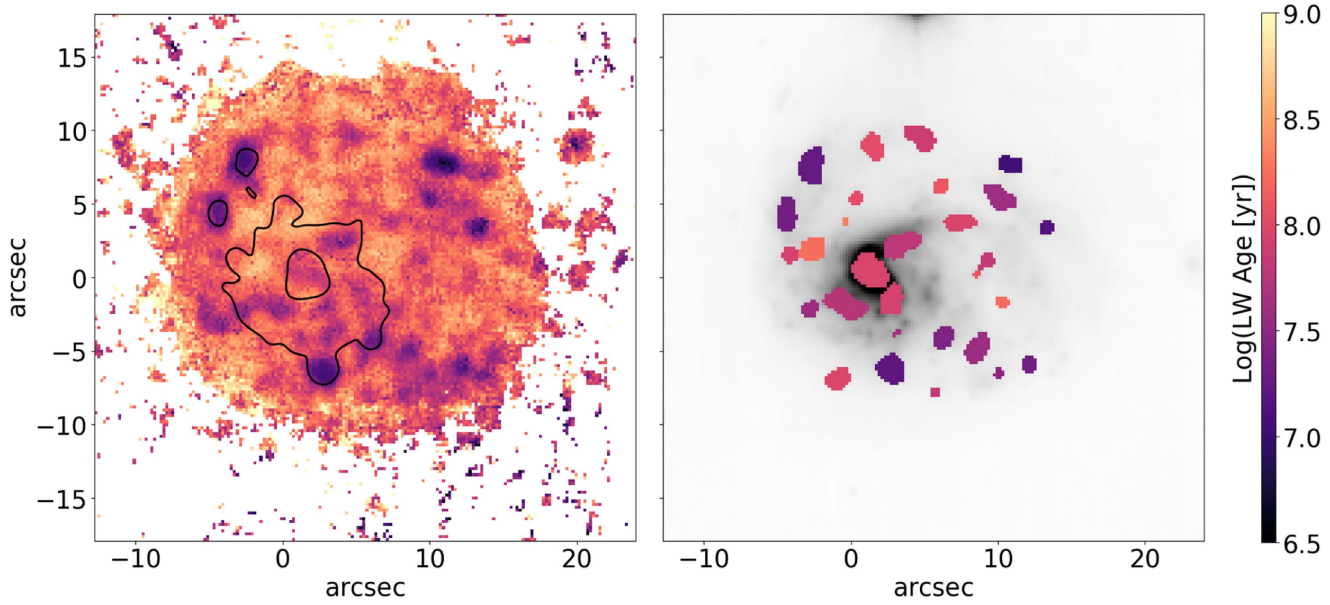

Figure 12. Luminosity-weighted age (LWA) map. Left: contours represent the original body (see Figure 14). Right: only regions corresponding to the 29 Hα knots identified in Figure 3 are color coded according to the median LWA of each knot. In the background, the white-light image of the galaxy (Figure 2) is shown for reference.

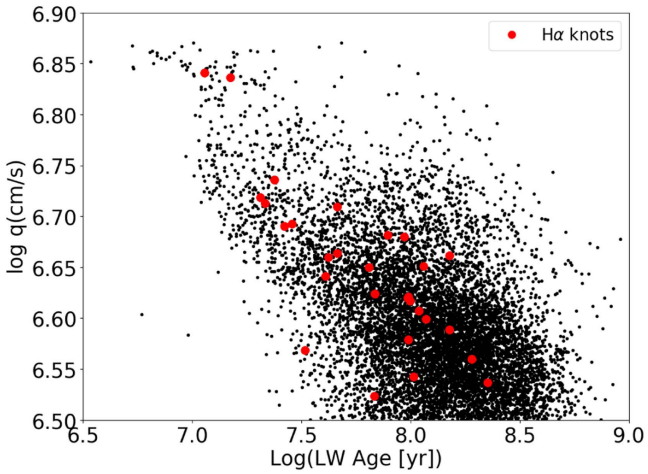

Figure 13. Correlation between the luminosity-weighted age and the parameter of ionization. The average values computed in each Hα knot are shown with red circles.

axisymmetric at intermediate time during the merger, but they do not look lopsided after the satellites have been completely accreted. Similarly, Bournaud et al. (2005) find that a 10:1 minor merger triggers significant lopsidedness, but this lasts typically no more than 500 Myr.

In contrast, flyby events can trigger lopsidedness (e.g., Mapelli et al. 2008), but at much lower level than gas accretion. Moreover, in case of a flyby, we should still see the companion close to P11695.

Hence, we need to invoke some other mechanism to explain the peculiarities of P11695.

4.2. Cold Gas Accretion Scenario

We propose a scenario in which the galaxy is being fed by a filament of cold ($T \leqslant 10^5$ K), low-metallicity gas, most probably flowing from the southwest side of the galaxy. This accretion increases the availability of gas pumping up the lopsidedness of the disk, igniting the formation of giant H II regions, influencing the gas motion, the conditions of star formation, and the metallicity of the galaxy.

In our observations, there are many indirect parts of evidence that are consistent with and point to the cold gas accretion scenario, as we describe in what follows.

4.2.1. Lopsidedness

P11695 is a spiral galaxy with very asymmetric features. It is lopsided and extends toward the west side much more than toward the east.

To quantify the lopsidedness in its surface density, we compute the Fourier transforms of the stellar mass surface density, obtained from SINOPSIS.

Following Bournaud et al. (2005), the surface density is decomposed as

$$\mu(r, \phi) = \mu_0(r) + \sum_m a_m(r)\cos(m\phi - \phi_m(r)), \qquad (1)$$

where the normalized strength of the Fourier component m is $A_m(r) = a_m/\mu_0(r)$. Thus, A_1 represents the normalized amplitude of the disk lopsidedness at a given radius. Values of $A_1 > 0.1$ indicate significant lopsidedness. The quantity ϕ_m denotes the position angle or the phase of the Fourier component m.

Figure 17 shows the amplitude $A_1(r)$ and the phase $\phi_1(r)$ versus radius r for the total stellar mass and the mass formed in two age bins ($t < 5.7 \times 10^8$ years and 5.7×10^8 years $< t < 1.4 \times 10^{10}$ years). Considering the total mass, P11695 appears to be significantly lopsided for $r > 10''$. The phase ϕ_1 is nearly constant for $r > 5''$, which is typical of most lopsided galaxies (see, e.g., Rix & Zaritsky 1995). Contrasting the curves for the two age bins, we find an increase in both the amplitude and the phase of the lopsidedness with time. This suggests that the west side of the galaxies developed in the recent epoch, $t < 5 \times 10^7$ years ago, in agreement with what is found in Figure 14.

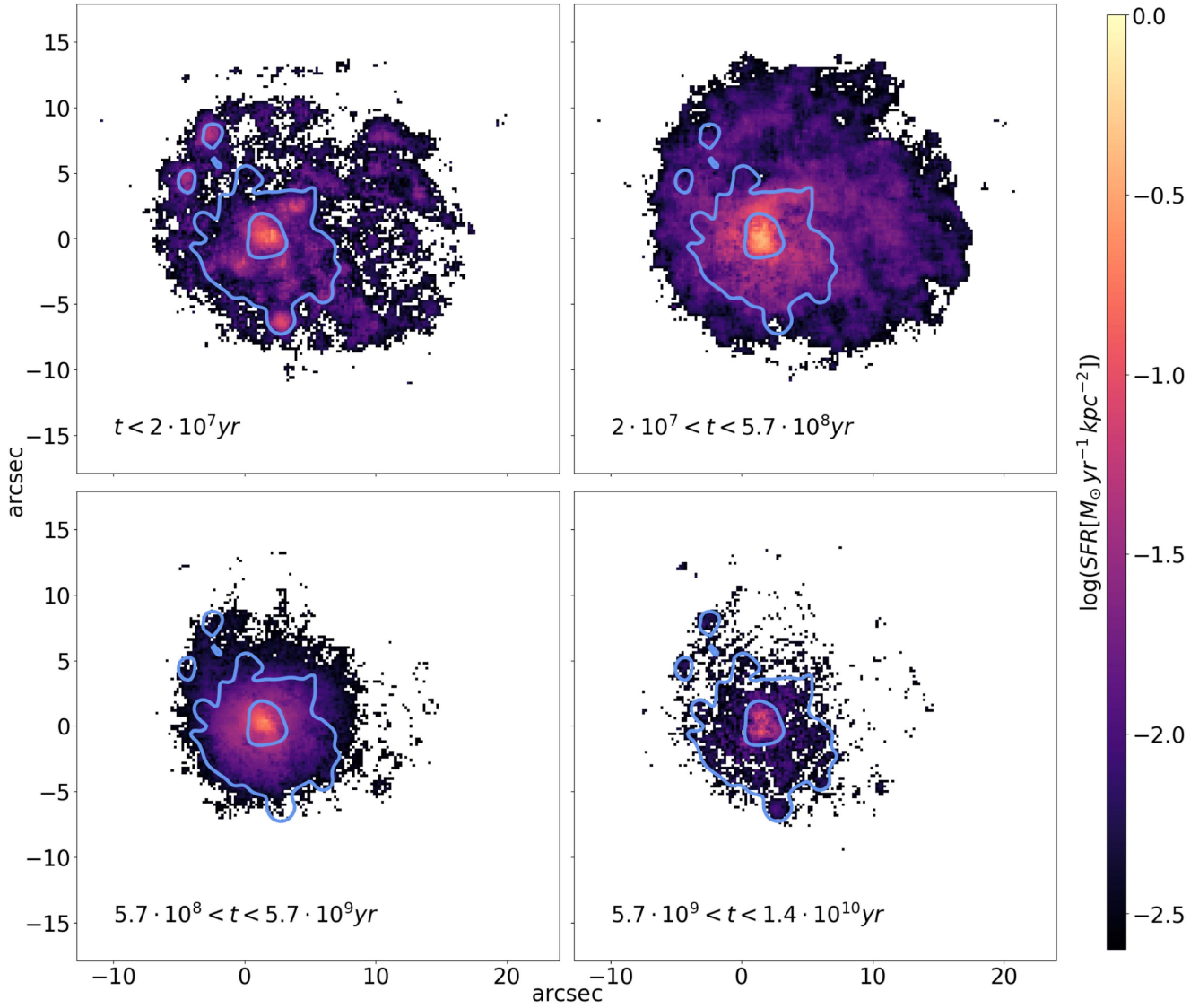

Figure 14. Stellar maps of different ages, illustrating the average star formation rate per kpc^2 during the last 2×10^7 years (top left), between 2×10^7 years and 5.7×10^8 years (top right), 5.7×10^8 years and 5.7×10^9 years (bottom left), and $>5.7 \times 10^9$ years ago (bottom right). Contours in all panels represent the original body, defined by the contours in the bottom right panel.

In principle, the asymmetric shape could be due to either accretion or a disk truncation, after a merger or due to a gas stripping. However, if the lopsidedness was due to mergers, we should also detect signs of the remnants in our spatially resolved spectroscopy (Mapelli et al. 2008), which is not the case. As for ram pressure, the galaxy should be located in a denser medium to feel the gas stripping, while we find no observational support for this hypothesis. In contrast, no observational evidence contradicts the gas inflow.

The simulations run by Bournaud et al. (2005) show that lopsidedness can result from cosmological accretion of gas on galactic disks, which can create strongly lopsided disks when this accretion is sufficiently asymmetrical. Simulations by, for example, Brook et al. (2008), Roškar et al. (2010), and Snaith et al. (2012) predict that misaligned gas structures are found to form and persist for many gigayears through the continued accretion of cold gas with misaligned angular momentum. In the absence of any continuous gas fuel, in an axisymmetric potential the gas will over time relax back into one of the preferred axes, becoming exactly co- or counterrotating with the stars (see also van de Voort et al. 2015).

This analysis therefore supports a scenario in which continuous gas accretion is feeding the galaxy, inducing the growth of the west side of the galaxy. Based on the stellar population analysis, we can date the beginning of the galaxy growth due to gas accretion to $<5.7 \times 10^8$ years ago.

4.2.2. Velocity Profiles

Jog (1997, 2002) showed that a galaxy showing spatial asymmetry would naturally show kinematical asymmetry. The two have to be casually connected in most cases. Instead, the gas and stellar components corotate and span the same velocity range in P11695. The gas kinematic shows a bending of the locus where velocities are negative in the external regions of the galaxy. Its convexity points toward the east. *N*-body/hydrodynamical simulations have shown that this U shape might be due to ram pressure stripping (Merluzzi et al. 2016), but it might also be related to gas accretion or galaxy

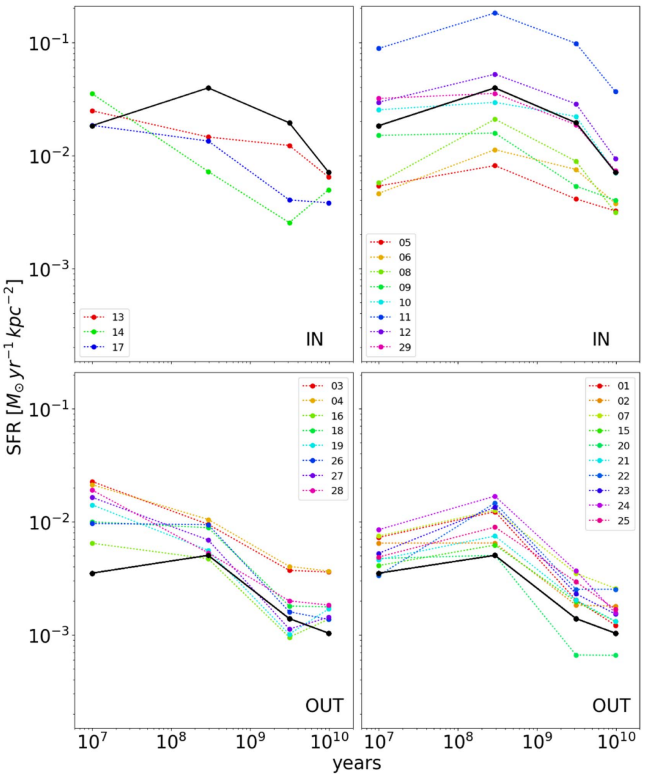

Figure 15. Star formation histories (average SFR in four age bins) per unit kpc^2 within (upper) and outside (bottom) the galaxy original body (see Figure 14), for each of the Hα knots (colored dashed lines). For the sake of clarity, the panels on the left show the Hα knots with rising SFH, and those on the right the Hα knots with declining SFH. The SFH for the entire galaxy within and outside the original body (black solid lines) is also reported for comparison.

interactions that produce lopsidedness (see, e.g., Sancisi et al. 2008, and references therein). In P11695, the bending is consistent with a scenario in which the gas is inflowing from the southwest with its own velocity and affects the gas velocity in its motion toward the center. The stellar kinematics might show a similar pattern, but this is less evident because this component is more bound than the gas, and therefore less easily disturbed.

The maps of velocity dispersions show that gas and stars have different levels of turbulence. Overall, the velocity dispersion of the gas decreases from the center toward the outskirts. In contrast, the stars have a more quiet motion in the core of the galaxy, but the velocity dispersion significantly increases toward the external regions. The SFH maps (Figure 14) have shown that the galaxy outskirts have formed in a recent epoch, and the motion of the newly formed stars might be influenced by the relative velocity and inclination of the inflowing gas.

4.2.3. Metallicity Gradients

P11695 has a generally low metallicity and a strong metallicity gradient. Compared to other gradients of late-type galaxies in the local universe (Pilyugin et al. 2014; Ho et al. 2015), P11695 has one of the steepest ones. Overall, the metallicity is higher in the core, in the northwest and southeast sides of the galaxy, while it is significantly lower in the southwest and northeast sides.

Mapelli et al. (2008), Oppenheimer et al. (2010), and Ma et al. (2016) suggest that strong metallicity gradients might support the cold gas accretion scenario: when particularly low-metallicity gas is detected in a galaxy halo, it is often claimed to be the accretion of the IGM filaments, because the pristine gas accreted through filaments is expected to be characterized by a lower metallicity than that of the target galaxy (see also Crighton et al. 2013; Lehner et al. 2013; Cooper et al. 2015, for higher z results).

Köppen & Hensler (2005) investigate the chemical evolution of galaxies that undergo an episode of massive and rapid accretion of metal-poor gas with models using both simplified and detailed nucleosynthesis recipes. Focusing on the effect of gas accretion on metallicity gradients in the last 2 Gyr, they find that during the infall, the oxygen abundance is decreased due to dilution of the galactic gas, followed after the infall by the evolution toward the closed-box relation. The large excursions in the gradient are reproduced if the mass of the infall is much larger than the mass of the gas present in the galaxy and the infall is greater than the SFR.

Radial metallicity gradients are instead expected to flatten once previously ejected gas begins to reaccrete. This is because metals that form and are ejected in a galaxy's core are mixed by the halo and redistributed to large radii. We should therefore be able to exclude a recycling of gas in P11695.

In principle, we could expect the region where the gas is inflowing to be much more metal-poor than the rest of the galaxy, with the result of having much more asymmetric gradients on the different sides of a same slit. This is true if the low-metallicity gas is able to form stars before having traveled across the galaxy and being mixed up with the existing gas. We can therefore estimate the time a particle would need to complete an orbit around the galaxy. As a first approximation, the orbital period is $P = 2\pi\frac{r}{v_c}$, with r the radius of the galaxy, and v_c the rotation velocity. From Figure 8 we obtain $v_c \sim 50$ km s^{-1} for $r > 3'' \sim = 2.7$ kpc. We adopt as inclination $i = 42$ deg. The orbital period becomes $\sim 2.5 \times 10^8$ years for $r = 3$ kpc and $\sim 8 \times 10^8$ years for $r = 10$ kpc. As in the northeast side of the galaxy, we do not observe strong metallicity gradients: the orbital periods suggest that the gas did not yet have time to complete an entire orbit and influence the metallicity of all newborn stars, and therefore it accreted in a later epoch. We only measure relatively low metallicity in the southwest and northeast sides of the galaxy. The former is the region where we hypothesize the gas is inflowing, that is, along the probable major axis of the original body of the galaxy.

4.2.4. Hα Knots

Another peculiarity of P11695 is the presence of many Hα knots. They are all on the main body and present elongated shapes.

Figure 18 shows the distribution of the properties in the knots compared to those in the main body. Median values obtained by considering all of the spaxels within each Hα knot agree with those obtained from the spectra integrated over the knots. Overall, the knots are dustier, have higher SFR values, younger ages, and higher ionization parameters than the rest of the galaxy, and have similar metallicity. A gradient in the properties of the knots, going from northeast to southwest, might be detected in all of the properties, with the exception of the two more external knots in the northwest area. Half of the current SFR is taking place in the Hα knots, which are therefore an important hotbed of new stars. In the last panel of Figure 18, we overplot the SFR distribution of H II regions of a

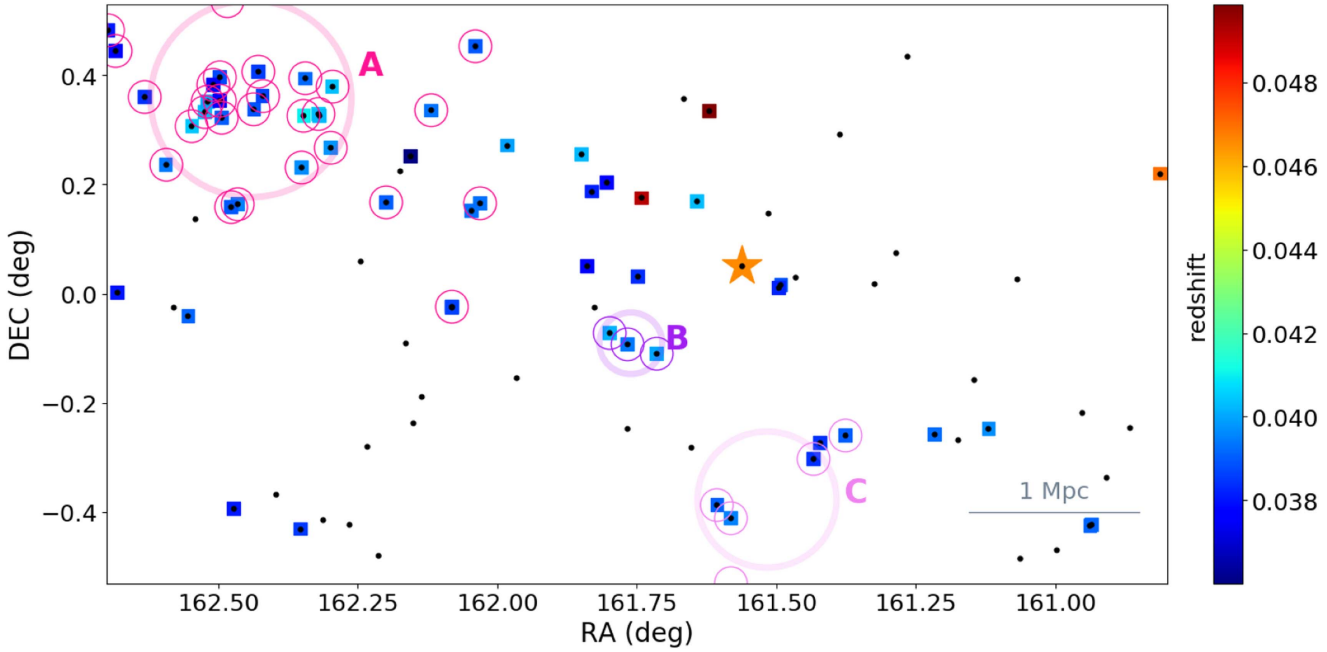

Figure 16. Position on the sky of galaxies around P11695 in the redshift range $0.025 < z < 0.07$ (black dots). Galaxies in the redshift range $0.035 < z < 0.05$ are color coded according to their redshift (squares). P11695 is indicated with an orange star. Galaxies belonging to groups identified by Calvi et al. (2011) and Tempel et al. (2012) are highlighted with open symbols (see Table 1 for details). Shaded circles indicate the virial radius of the groups. The scale in the bottom right corner shows 1 Mpc at the redshift of P11695.

Table 1
Properties of the Groups around P11695

ID	Ngal	z	R.A. (J2000)	Decl. (J2000)	Rvir (Mpc)	σ (km s^{-1})
A	32	0.04036	162.44151	0.3568	0.51	245.8
B	3	0.04106	161.76073	−0.09061	0.16	118.1
C	5	0.04008	161.51663	−0.3767	0.35	134.1

Note. Data taken from Tempel et al. (2012).

sample of 52 nearby galaxies, studied by Alonso-Herrero & Knapen (2001). These authors provide the brightest, the median, and the faintest Hα luminosities of the circumnuclear H II regions. We converted their luminosities to SFRs and find that indeed the Hα knots in P11695 are systematically larger than both the typical and brightest H II regions in other galaxies.

Considering the SFH of the Hα knots, we find that most of them follow the trend of the entire galaxy, except for the Hα knots located in the southwest region. They all have rising SFHs, suggesting that a large amount of fuel for star formation is available in this region of P11695.

Even though clumpy galaxies in the local universe are not as common as at higher redshift (e.g., Genzel et al. 2006; Elmegreen et al. 2007; Agertz et al. 2009), samples at redshifts similar to that of P11695 have been studied, for example, by Smith et al. (2001) and Garland et al. (2015). Overall, the continuous appearance of clump–cluster galaxies throughout a wide range of redshifts means that disk galaxies start forming over an extended period of time.

We are not able to state whether the knots we observe are the first knots formed in the galaxy or if they are an nth generation of

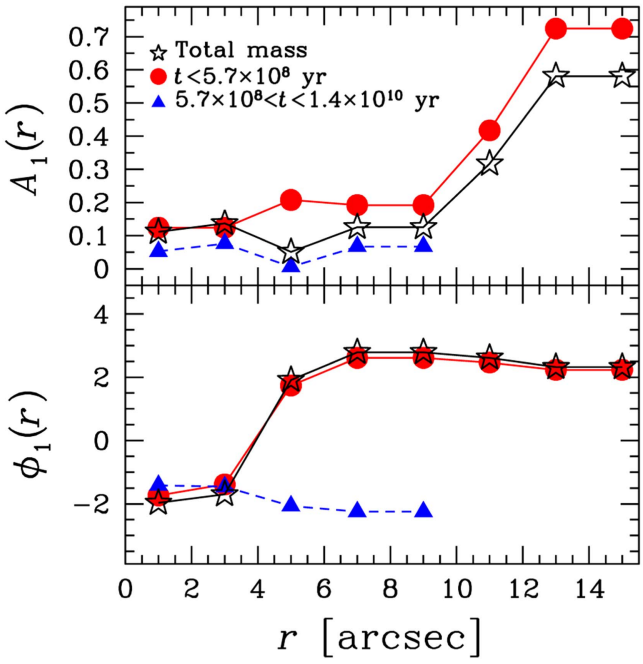

Figure 17. Normalized amplitude of the disk lopsidedness ($A_1(r)$, top) and phase of the Fourier component $m = 1$ ($\phi_1(r)$, bottom) as a function of the radius r, for the total mass (black stars), the mass formed $<5 \times 10^7$ years ago (red circles), and the mass formed in the range 5.7×10^8 years $< t < 1.4 \times 10^{10}$ years (blue triangles).

knots. For example, Elmegreen et al. (2007) claim that the clump–cluster phase lasts for 0.5–1 Gyr and occurs only once during the life of a galaxy, unless there is a significant accretion event later. In contrast, simulations by Noguchi (1999) do not exclude the possibility that new generations of knots are easily formed.

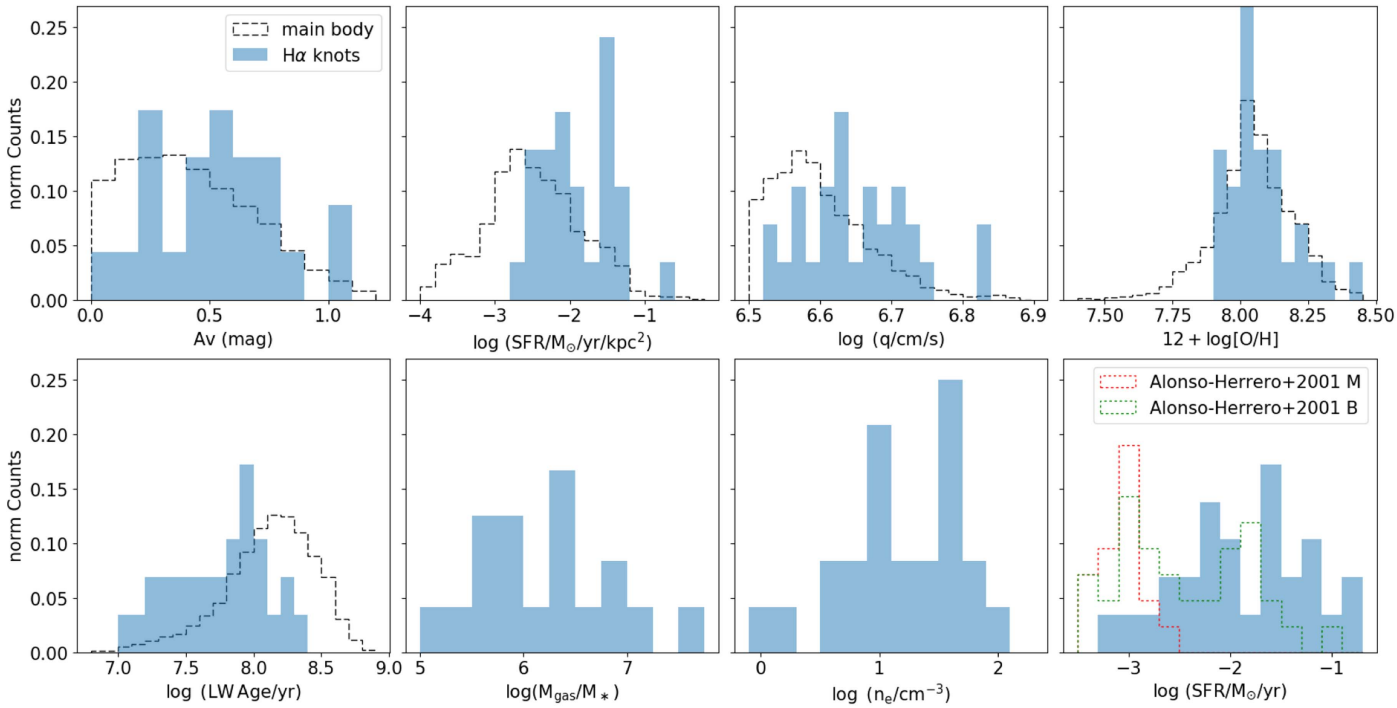

Figure 18. Normalized distribution of the properties of the Hα knots, compared to that of the galaxy main body (when meaningful). The A_V, SFR per unit kpc^2, parameter of ionization, metallicity, luminosity-weighted age, gas mass, electron density, and SFR are shown. In the bottom right panel, we report for comparison the SFR distributions obtained from the Hα luminosity as measured by Alonso-Herrero & Knapen (2001) for H II regions in nearby galaxies. Estimates using only the brightest (B) and median (M) Hα luminosities are shown.

The explanation for the existence of these knots is that when a disk becomes sufficiently massive through accretion (through cold gas inflow in our case), giant clumps form at the local Jeans mass by gravitational instabilities. This induces a disk fragmentation, without destroying the disk. The mass of the clumps therefore depends on the turbulent Jeans mass. As turbulent speeds decrease relative to the rotation speed, clump masses decrease relative to the galaxy mass; then their interactions and migrations toward the bulge become less severe.

As described in detail in Paper I, we can compute the gas mass of each star-forming region from the Hα luminosity (Boselli et al. 2016), after having estimated the electron density. To do that, we follow the relation presented in Proxauf et al. (2014) that is based on the $R = [\mathrm{S\,II}]6717/[\mathrm{S\,II}]6737$ line ratio and is valid in the range $0.4 < \mathrm{R} < 1.435$. We find 24 out of 29 knots have a $[\mathrm{S\,II}]6716/[\mathrm{S\,II}]6732$ ratio in the range where the density calibration applies, while the others have ratio values larger than 1.44, which suggest that their density is below 10 cm^{-3}. The distribution of their ionized gas densities is shown in Figure 18. Most of the measured densities are between 3 and 100 cm^{-3}, with a median of 19 cm^{-3}. The derived ionized gas mass distribution is also shown in Figure 18. Most of the knots have masses in the range 10^5–$10^{7.5}$ $M_\odot$, with a median of 7.9×10^5 $M_\odot$. Summing up the gas mass in these knots, we obtain $\sim 10^8$ $M_\odot$. This value has to be taken as a lower limit to the total ionized gas mass, given that the contributions of the knots with no density estimate and of the diffuse line emission are not taken into account.

Note that if major interactions were occurring, the resulting galaxy would likely include a highly concentrated central starburst, not smaller clumps of star formation spread throughout.

4.2.5. Star-forming Properties

The typical luminosity-weighted age of P11695 is $10^{8\text{–}8.5}$ years, but the galaxy is characterized by a large number of much younger regions ($\sim 10^7$ years). In particular, Figure 12 suggests the existence of a trail of very young stars starting from the southwest side, extending toward the east and continuing on the north side toward the west. It is tempting to interpret this as the path of new gas inflowing and then orbiting around the original body of the galaxy.

The analysis of the SFHs showed that at the early stage of its formation, P11695 probably was a much more symmetric object. The lopsidedness seems to have started to develop at later times, especially in the second-youngest bin. The measurement of the amplitude of the lopsidedness confirms this finding. In the youngest age bin, the SFR is declining, and the outskirts of the galaxies form stars at a lower level. Also, these findings are consistent with a scenario according to which after its formation, P11695 has been fed by a gas inflow, leading to a more massive extension of the galaxy on the west side. The decrease in star formation observed today might suggest that currently the gas flow is feeding the galaxy at a lower rate.

4.3. Final Remarks

P11695 has been observed by the ALFALFA survey (Giovanelli et al. 2005).[9] Given the low resolution of the observations, we cannot characterize the lopsidedness, but we can obtain an estimate of its H I mass, which can be considered as the raw fuel for star formation and a lower limit of the accreted gas mass, as a large fraction of it has already formed

[9] The galaxy is not in the publicly released ALFALFA catalog, since its S/N is below the adopted limit (S/N > 6).

stars. The inferred $M_{\rm H\,I}$ is $1.03 \pm 0.2 \times 10^{10}\,M_{\odot}$ (D. Stark 2017, private communication), entailing an $M_{\rm H\,I}/M_{*} \sim 0.8$. Comparing its position on the $M_{\rm H\,I}/M_{*}$ versus M_{*} plane to that of galaxies at $z = 0$ drawn from the RESOLVE survey (Stark et al. 2016), we find it lies on the upper envelope of the relation (see also Putman 2017), suggesting its ratio is higher than the typical one for galaxies with similar stellar mass. P11695 therefore still has a large reservoir of unprocessed gas.

Considering the SFR of the galaxy ($3.27\ M_{\odot}\ {\rm yr}^{-1}$), the star formation efficiency (SFR/$M_{\rm gas}$) turns out to be $0.31\ {\rm Gyr}^{-1}$, which gives us a timescale of the gas consumption. Bournaud et al. (2005) simulate accretion rates of the order $\sim$3–9 $M_{\odot}\ {\rm yr}^{-1}$ for $\sim$2 Gyr (see also van de Voort & Schaye 2012), yielding a total accreted mass of $0.6–1.8 \times 10^{10}\,M_{\odot}$, which is the same order of magnitude as our estimates. For comparison, in the Milky Way, gas that is clearly infalling is observed at 1–15 kpc above the disk. The actual rate of accretion depends on the 3D motions of the gas and the full extent of the accreting layer, but the rates calculated are $\sim$0.1–0.4 $M_{\odot}\ {\rm yr}^{-1}$ for the coldest gas (Putman et al. 2012), and closer to $\sim 1\,M_{\odot}\ {\rm yr}^{-1}$ when the ionized gas is included (Lehner & Howk 2011). In M33, a direct detection of gas accretion yields an accretion rate of $\sim 2.9\,M_{\odot}\ {\rm yr}^{-1}$. This amount is relatively large for this small galaxy and may be further evidence for the infall of fuel being intermittent in nature (Zheng et al. 2017).

Taking into account the adopted inclination of P11695, we can suppose a U-shaped warp for the galaxy visible in the most external regions. The possible presence of the warp could be indicated also by the fact that the velocity field indicates a change of the apparent major axis from the inner to the outer region of the galaxy. This velocity distribution can be represented by annular rings in circular motion, progressively more inclined at larger radii (van der Kruit & Allen 1978). Sancisi (1976) and Binney (1992) have emphasized that warps occur in apparently isolated galaxies. They conclude that if the generator of the warps is invisible, this could be outer gas accretion (see also López-Corredoira et al. 2002; Bournaud et al. 2005; Kamphuis et al. 2013, for more recent results), consistent with our general interpretation.

Reichard et al. (2009) connected the lopsidedness of 25,000 star-forming galaxies from SDSS to metallicity. They found that at a fixed mass, the more metal-poor galaxies turn out to be more lopsided, extending the morphology–metallicity relation to the full population of star-forming galaxies. This result might explain why P11695 lies away from the Tremonti et al. (2004) mass–metallicity relation. Reichard et al. (2009) interpret their result in the context of a gas accretion triggering scenario. Indeed, the accreted gas is metal-poor (e.g., Dekel et al. 2009; van de Voort & Schaye 2012) and induces off-center, giant star-forming clumps that gradually migrate toward the disk centers (Ceverino et al. 2010; Mandelker et al. 2014). The giant star-forming clumps may be born in situ (if the accreted gas builds up the gas reservoir in the disk to a point where disk instabilities set in and trigger star formation) or ex situ (if already-formed clumps are incorporated into the disk). In both cases, a significant part of the star formation in the disks occurs in these giant clumps. As a result of the whole process, the gas accretion produces bright, off-center starbursts that increase the lopsidedness of the host disk. This explanation also suits our observational results.

Unfortunately, we are not able to get direct observations of this gas flow. As discussed, for example, by Rubin (2016), an unequivocal evidence of gas flow toward a source is the detection of absorption lines in a galaxy's spectrum that show a velocity shift with respect to its rest frame. The continuum spectrum can be either a higher redshift background source or the host galaxy itself. This technique is sensitive to the inflow of material over a broad range of densities and temperatures. Even though we found a high-redshift ($z = 0.458$) galaxy in the MUSE field of view, $\sim$40′ northwest from P11695, its flux is too weak to detect any possible sign of absorption by the gas inflow.

5. Summary and Conclusions

GASP (Gas Stripping Phenomena in galaxies with MUSE) is an ongoing ESO Large program with the MUSE/VLT to study the causes and effects of gas-removal processes in galaxies in different environments. Within the sample, we identified a galaxy that is likely undergoing accretion through a cold gas filament coming from the southwest side of the galaxy. In this paper we analyze its spatially resolved properties that indirectly support this scenario.

P11695 is an isolated spiral galaxy at $z = 0.04648$ showing a marked lopsidedness in the light distribution. Such lopsidedness developed $<6 \times 10^{8}$ years ago. The gas and the stars are corotating around the same axis, but the velocity field of the gas bends in the outskirts, as if new gas has been infalling with a different orientation and velocity.

P11695 presents steep metallicity gradients, as expected from simulations when cold accretion of low-metallicity gas is occurring (e.g., Mapelli et al. 2008). P11695 has low levels of dust ($A_V < 1$mag), a low ionization parameter value ($\log(q) \sim 6.5$), and a quite young luminosity-weighted age ($\log({\rm LWA}) \sim 8.4$). Both the luminosity-weighted age and parameter of ionization maps are very patchy, and we found a close correspondence between the two. A trail of very young stars ($\log({\rm LWA}) \sim 7$) visible across the galaxy might trace the path of the new gas. Another important characteristic is the presence of 29 elongated Hα knots on the galaxy disk. These knots have systematically lower metallicity, younger ages, and higher ionization parameters than the rest of the galaxy.

Finally, it is worth stressing again that this galaxy was selected because it showed signs that could be indicative of stripping, so it emerges that, in optical images, gas stripping and gas accretion can present similar features. Within the GASP sample, we recently detected other galaxies not belonging to any structure whose properties might resemble those of P11695. In a subsequent paper, we will characterize this whole sample, in order to state whether all isolated galaxies that present signatures suggestive of gas stripping are on the contrary still accreting gas.

We thank the anonymous referee whose comments helped us to strengthen the manuscript. This work is based on observations collected at the European Organisation for Astronomical Research in the southern hemisphere under ESO program 196.B-0578. This work made use of the KUBEVIZ software, which is publicly available at http://www.mpe.mpg.de/~dwilman/kubeviz/. We thank Marco Ajello, Valentina La Parola, and Fabrizio Nicastro for useful discussions. We thank the ALFALFA team for sharing their private catalog and David Stark for providing us with the H I measurements and for stimulating discussions. We are grateful to Joe Liske, Simon Driver, and the whole MGC collaboration

for making their data set easily available, and to Rosa Calvi for her valuable work on the PM2GC. We acknowledge financial support from PRIN-INAF 2014. B.V. acknowledges the support from an Australian Research Council Discovery Early Career Researcher Award (PD0028506). M.M. acknowledges financial support from the Italian Ministry of Education, University and Research (MIUR) through grant FIRB 2012 RBFR12PM1F, from INAF through grant PRIN-2014-14 (Star Formation and Evolution in Galactic Nuclei), and from the MERAC Foundation. J.F. acknowledges financial support from UNAM-DGAPA-PAPIIT IA104015 grant, México. This work was cofunded under the Marie Curie Actions of the European Commission (FP7-COFUND).

Facility: VLT(MUSE).

Software: KUBEVIZ, ESOREX, SINOPSIS, IRAF, CLOUDY, pyqz, IDL, Python.

ORCID iDs

Benedetta Vulcani https://orcid.org/0000-0003-0980-1499
Bianca M. Poggianti https://orcid.org/0000-0001-8751-8360
Alessia Moretti https://orcid.org/0000-0002-1688-482X
Jacopo Fritz https://orcid.org/0000-0002-7042-1965
Daniela Bettoni https://orcid.org/0000-0002-4158-6496
Marco Gullieuszik https://orcid.org/0000-0002-7296-9780
Callum Bellhouse https://orcid.org/0000-0002-6179-8007

References

Agertz, O., Teyssier, R., & Moore, B. 2009, MNRAS, 397, L64
Ahn, C. P., Alexandroff, R., Allende Prieto, C., et al. 2012, ApJS, 203, 21
Alonso-Herrero, A., & Knapen, J. H. 2001, AJ, 122, 1350
Angiras, R. A., Jog, C. J., Dwarakanath, K. S., & Verheijen, M. A. W. 2007, MNRAS, 378, 276
Ann, H. B., & Park, J.-C. 2006, NewA, 11, 293
Argudo-Fernández, M., Verley, S., Bergond, G., et al. 2015, A&A, 578, A110
Baldwin, J. E., Lynden-Bell, D., & Sancisi, R. 1980, MNRAS, 193, 313
Battaner, E., Florido, E., & Sanchez-Saavedra, M. L. 1990, A&A, 236, 1
Beale, J. S., & Davies, R. D. 1969, Natur, 221, 531
Binney, J. 1992, ARA&A, 30, 51
Block, D. L., Bertin, G., Stockton, A., et al. 1994, A&A, 288, 365
Boselli, A., Cuillandre, J. C., Fossati, M., et al. 2016, A&A, 587, A68
Bosma, A. 1981, AJ, 86, 1791
Bottema, R. 1995, A&A, 295, 605
Bournaud, F., Combes, F., Jog, C. J., & Puerari, I. 2005, A&A, 438, 507
Briggs, F. H. 1990, ApJ, 352, 15
Brook, C. B., Governato, F., Quinn, T., et al. 2008, ApJ, 689, 678
Brooks, A. M., Governato, F., Quinn, T., Brook, C. B., & Wadsley, J. 2009, ApJ, 694, 396
Bundy, K., Bershady, M. A., Law, D. R., et al. 2015, ApJ, 798, 7
Byrd, G., & Valtonen, M. 1990, ApJ, 350, 89
Cappellari, M., & Copin, Y. 2003, MNRAS, 342, 345
Cappellari, M., & Emsellem, E. 2004, PASP, 116, 138
Calvi, R., Poggianti, B. M., & Vulcani, B. 2011, MNRAS, 416, 727
Cardelli, J. A., Clayton, G. C., & Mathis, J. S. 1989, ApJ, 345, 245
Ceverino, D., Dekel, A., & Bournaud, F. 2010, MNRAS, 404, 2151
Chabrier, G. 2003, PASP, 115, 763
Combes, F., Boisse, P., Mazure, A., & Blanchard, A. 2004, Galaxies and Cosmology (New York: Springer)
Cooper, T. J., Simcoe, R. A., Cooksey, K. L., O'Meara, J. M., & Torrey, P. 2015, ApJ, 812, 58
Cortese, L., Fogarty, L. M. R., Ho, I.-T., et al. 2014, ApJL, 795, L37
Covington, M. D., Kassin, S. A., Dutton, A. A., et al. 2010, ApJ, 710, 279
Cresci, G., Mannucci, F., Maiolino, R., et al. 2010, Natur, 467, 811
Crighton, N. H. M., Hennawi, J. F., & Prochaska, J. X. 2013, ApJL, 776, L18
Croom, S. M., Lawrence, J. S., Bland-Hawthorn, J., et al. 2012, MNRAS, 421, 872
Dekel, A., & Birnboim, Y. 2006, MNRAS, 368, 2
Dekel, A., Birnboim, Y., Engel, G., et al. 2009, Natur, 457, 451
Dopita, M. A., Sutherland, R. S., Nicholls, D. C., Kewley, L. J., & Vogt, F. P. A. 2013, ApJS, 208, 10
Driver, S. P., Liske, J., Cross, N. J. G., De Propris, R., & Allen, P. D. 2005, MNRAS, 360, 81
Dubinski, J., & Kuijken, K. 1995, ApJ, 442, 492
Elmegreen, D. M., Elmegreen, B. G., Ravindranath, S., & Coe, D. A. 2007, ApJ, 658, 763
Fasano, G., Marmo, C., Varela, J., et al. 2006, A&A, 445, 805
Faucher-Giguere, C.-A. 2011, BAAS, 43, 119.03
Faucher-Giguère, C.-A., Kereš, D., & Ma, C.-P. 2011, MNRAS, 417, 2982
Fossati, M., Fumagalli, M., Boselli, A., et al. 2016, MNRAS, 455, 2028
Fritz, J., Moretti, A., Poggianti, B., et al. 2017, ApJ, 848, 132
Fritz, J., Poggianti, B. M., Bettoni, D., et al. 2007, A&A, 470, 137
Garland, C. A., Pisano, D. J., Mac Low, M.-M., et al. 2015, ApJ, 807, 134
Genel, S., Dekel, A., & Cacciato, M. 2012, MNRAS, 425, 788
Genzel, R., Tacconi, L. J., Eisenhauer, F., et al. 2006, Natur, 442, 786
Giovanelli, R., Haynes, M. P., Kent, B. R., et al. 2005, AJ, 130, 2598
Gullieuszik, M., Poggianti, B., Fasano, G., et al. 2015, A&A, 581, A41
Gullieuszik, M., Poggianti, B. M., Moretti, A., et al. 2017, ApJ, 846, 27
Gunn, J. E., & Gott, J. R., III 1972, ApJ, 176, 1
Haynes, M. P., van Zee, L., Hogg, D. E., Roberts, M. S., & Maddalena, R. J. 1998, AJ, 115, 62
Ho, I.-T., Kudritzki, R.-P., Kewley, L. J., et al. 2015, MNRAS, 448, 2030
Hobbs, A., Read, J., & Nicola, A. 2015, MNRAS, 452, 3593
Huang, S., & Carlberg, R. G. 1997, ApJ, 480, 503
Ideta, M. 2002, ApJ, 568, 190
Jog, C. J. 1997, ApJ, 488, 642
Jog, C. J. 2002, A&A, 391, 471
Jog, C. J., & Combes, F. 2009, PhR, 471, 75
Junqueira, S., & Combes, F. 1996, A&A, 312, 703
Kamphuis, P., Rand, R. J., Józsa, G. I. G., et al. 2013, MNRAS, 434, 2069
Kassin, S. A., Weiner, B. J., Faber, S. M., et al. 2007, ApJL, 660, L35
Kauffmann, G., Heckman, T. M., Tremonti, C., et al. 2003, MNRAS, 346, 1055
Kennicutt, R. C., Jr. 1998, ARA&A, 36, 189
Kereš, D., Katz, N., Weinberg, D. H., & Davé, R. 2005, MNRAS, 363, 2
Kewley, L. J., & Ellison, S. L. 2008, ApJ, 681, 1183
Kewley, L. J., Groves, B., Kauffmann, G., & Heckman, T. 2006, MNRAS, 372, 961
Kewley, L. J., Heisler, C. A., Dopita, M. A., & Lumsden, S. 2001, ApJS, 132, 37
Kim, J. H., Peirani, S., Kim, S., et al. 2014, ApJ, 789, 90
Köppen, J., & Hensler, G. 2005, A&A, 434, 531
Kuijken, K., & Garcia-Ruiz, I. 2001, in ASP Conf. Ser. 230, Galaxy Disks and Disk Galaxies, ed. J. G. Funes & E. M. Corsini (San Francisco, CA: ASP), 401
Lehner, N., & Howk, J. C. 2011, Sci, 334, 955
Lehner, N., Howk, J. C., Tripp, T. M., et al. 2013, ApJ, 770, 138
Levine, S. E., & Sparke, L. S. 1998, ApJL, 496, L13
Liske, J., Lemon, D. J., Driver, S. P., Cross, N. J. G., & Couch, W. J. 2003, MNRAS, 344, 307
López-Corredoira, M., Betancort-Rijo, J., & Beckman, J. E. 2002, A&A, 386, 169
Ma, X., Hopkins, P. F., Faucher-Giguère, C.-A., et al. 2016, MNRAS, 456, 2140
Mandelker, N., Dekel, A., Ceverino, D., et al. 2014, MNRAS, 443, 3675
Mapelli, M., Moore, B., & Bland-Hawthorn, J. 2008, MNRAS, 388, 697
Matthews, L. D., van Driel, W., & Gallagher, J. S., III 1998, AJ, 116, 2196
Merluzzi, P., Busarello, G., Dopita, M. A., et al. 2016, MNRAS, 460, 3345
Mihalas, D., & Binney, J. 1981, Sci, 214, 829
Moustakas, J., Kennicutt, R. C., Jr., Tremonti, C. A., et al. 2010, ApJS, 190, 233
Nelson, D., Genel, S., Pillepich, A., et al. 2016, MNRAS, 460, 2881
Nelson, D., Vogelsberger, M., Genel, S., et al. 2013, MNRAS, 429, 3353
Nishiura, S., Shimada, M., Ohyama, Y., Murayama, T., & Taniguchi, Y. 2000, AJ, 120, 1691
Noeske, K. G., Faber, S. M., Weiner, B. J., et al. 2007, ApJL, 660, L47
Noguchi, M. 1999, AdSpR, 23, 1121
Noordermeer, E., Sparke, L. S., & Levine, S. E. 2001, MNRAS, 328, 1064
Ocvirk, P., Pichon, C., & Teyssier, R. 2008, MNRAS, 390, 1326
Oppenheimer, B. D., Davé, R., Kereš, D., et al. 2010, MNRAS, 406, 2325
Paccagnella, A. 2018, MNRAS, submitted
Pilyugin, L. S., Grebel, E. K., & Kniazev, A. Y. 2014, AJ, 147, 131
Poggianti, B. M., Fasano, G., Omizzolo, A., et al. 2016, AJ, 151, 78
Poggianti, B. M., Moretti, A., Gullieuszik, M., et al. 2017, ApJ, 844, 48
Proxauf, B., Öttl, S., & Kimeswenger, S. 2014, A&A, 561, A10

Putman, M. E. 2017, Astrophysics and Space Science Library, 430, 1
Putman, M. E., Peek, J. E. G., & Joung, M. R. 2012, ARA&A, 50, 491
Reichard, T. A., Heckman, T. M., Rudnick, G., et al. 2009, ApJ, 691, 1005
Reshetnikov, V., & Combes, F. 1998, A&A, 337, 9
Revaz, Y., & Pfenniger, D. 2001, in ASP Conf. Ser. 240, Gas and Galaxy Evolution, ed. J. E. Hibbard, M. Rupen, & J. H. van Gorkom (San Francisco, CA: ASP), 278
Richter, O.-G., & Sancisi, R. 1994, A&A, 290, 9
Rix, H.-W., & Zaritsky, D. 1995, ApJ, 447, 82
Roškar, R., Debattista, V. P., Brooks, A. M., et al. 2010, MNRAS, 408, 783
Rubin, K. H. R. 2016, arXiv:1612.00805
Rubin, V. C., Hunter, D. A., & Ford, W. K., Jr. 1991, ApJS, 76, 153
Rubin, V. C., Waterman, A. H., & Kenney, J. D. P. 1999, AJ, 118, 236
Rupke, D. S. N., Kewley, L. J., & Chien, L.-H. 2010, ApJ, 723, 1255
Sánchez, S. F., Kennicutt, R. C., Gil de Paz, A., et al. 2012, A&A, 538, A8
Sánchez, S. F., Rosales-Ortega, F. F., Iglesias-Páramo, J., et al. 2014, A&A, 563, A49
Sanchez-Saavedra, M. L., Battaner, E., & Florido, E. 1990, MNRAS, 246, 458
Sancisi, R. 1976, A&A, 53, 159
Sancisi, R., Fraternali, F., Oosterloo, T., & van der Hulst, T. 2008, A&ARv, 15, 189
Schoenmakers, R. H. M., Franx, M., & de Zeeuw, P. T. 1997, MNRAS, 292, 349
Schwarzkopf, U., & Dettmar, R.-J. 2001, A&A, 373, 402
Sellwood, J. A. 2013, in Dynamics of Disks and Warps, ed. T. D. Oswalt & G. Gilmore, 923
Semelin, B., & Combes, F. 2005, A&A, 441, 55
Sharp, R. G., & Bland-Hawthorn, J. 2010, ApJ, 711, 818
Silk, J., & Mamon, G. A. 2012, RAA, 12, 917
Smith, A. M., Collins, N. R., Waller, W. H., et al. 2001, ApJ, 546, 829
Snaith, O. N., Gibson, B. K., Brook, C. B., et al. 2012, MNRAS, 425, 1967
Sofue, Y., & Rubin, V. 2001, ARA&A, 39, 137
Sparke, L. S., & Casertano, S. 1988, MNRAS, 234, 873
Springel, V. 2010, MNRAS, 401, 791
Stark, D. V., Kannappan, S. J., Eckert, K. D., et al. 2016, ApJ, 832, 126
Strauss, M. A., Weinberg, D. H., Lupton, R. H., et al. 2002, AJ, 124, 1810
Swaters, R. A., Schoenmakers, R. H. M., Sancisi, R., & van Albada, T. S. 1999, MNRAS, 304, 330
Tempel, E., Tago, E., & Liivamägi, L. J. 2012, A&A, 540, A106
Toomre, A. 1983, in IAU Symp. 100, Internal Kinematics and Dynamics of Galaxies, ed. E. Athanassoula (Cambridge: Cambridge Univ. Press), 177
Torrey, P., Vogelsberger, M., Sijacki, D., Springel, V., & Hernquist, L. 2012, MNRAS, 427, 2224
Tremonti, C. A., Heckman, T. M., Kauffmann, G., et al. 2004, ApJ, 613, 898
van de Voort, F., Davis, T. A., Kereš, D., et al. 2015, MNRAS, 451, 3269
van de Voort, F., & Schaye, J. 2012, MNRAS, 423, 2991
van de Voort, F., Schaye, J., Booth, C. M., Haas, M. R., & Dalla Vecchia, C. 2011, MNRAS, 414, 2458
van der Kruit, P. C. 2007, A&A, 466, 883
van der Kruit, P. C., & Allen, R. J. 1978, ARA&A, 16, 103
Véron-Cetty, M.-P., & Véron, P. 2003, A&A, 412, 399
Véron-Cetty, M.-P., & Véron, P. 2006, A&A, 455, 773
Walker, I. R., Mihos, J. C., & Hernquist, L. 1996, ApJ, 460, 121
Weinberg, M. D. 1995, ApJL, 455, L31
Weiner, B. J., Willmer, C. N. A., Faber, S. M., et al. 2006, ApJ, 653, 1027
Wilcots, E. M., & Prescott, M. K. M. 2004, AJ, 127, 1900
Young, L. M., Rosolowsky, E., van Gorkom, J. H., & Lamb, S. A. 2006, ApJ, 650, 166
Zaritsky, D., Kennicutt, R. C., Jr., & Huchra, J. P. 1994, ApJ, 420, 87
Zaritsky, D., & Rix, H.-W. 1997, ApJ, 477, 118
Zheng, Y., Peek, J. E. G., Werk, J. K., & Putman, M. E. 2017, ApJ, 834, 179

The Astrophysical Journal, 859:76 (4pp), 2018 May 20 https://doi.org/10.3847/1538-4357/aabe94

Erratum: "GASP. VII. Signs of Gas Inflow onto a Lopsided Galaxy" (2018, ApJ, 852, 94)

Benedetta Vulcani[1,2], Bianca M. Poggianti[2], Alessia Moretti[2], Michela Mapelli[2], Giovanni Fasano[2], Jacopo Fritz[3], Yara Jaffé[4], Daniela Bettoni[2], Marco Gullieuszik[2], and Callum Bellhouse[4,5]
[1] School of Physics, University of Melbourne, VIC 3010, Australia
[2] INAF, Osservatorio Astronomico di Padova, Vicolo Osservatorio 5, I-35122 Padova, Italy
[3] Instituto de Radioastronomía y Astrofísica, UNAM, Campus Morelia, A.P. 3-72, C.P. 58089, Mexico
[4] European Southern Observatory, Alonso de Cordova 3107, Vitacura, Casilla 19001, Santiago de Chile, Chile
[5] University of Birmingham School of Physics and Astronomy, Edgbaston, Birmingham, UK
Received 2018 April 13; published 2018 May 24

After the published paper was accepted, and during the preparation of the proof, an issue internal to the Publishing team occurred and a preliminary version of the manuscript was sent to the typesetters. As a result, the published paper does not correspond to the accepted version.

While none of the conclusions and trends presented are affected, Figures 9, 10, 11, 13, and 18 in the published paper and the related text need to be amended. Values in the text should be updated accordingly in a few sentences as follows:

In Section 3.5.

The spatial distribution of the ionization parameter for P11695 is presented in Figure 1. It is generally low, ranging from $6.6 < \log(q) < 7.3$. This is in agreement with other galaxies in the GASP survey (Gullieuszik et al. 2017; Poggianti et al. 2017), even though in this case a clear clumpy pattern emerges, while in other galaxies a more smooth distribution is observed. Hα knots tend to have a systematically large value of q: the median value integrated across the entire galaxy is 6.8, while the median value in the Hα knots is 7.

Figure 2 shows that the spatially resolved metallicity ranges between $8.3 < 12 + \log(\mathrm{O/H}) < 9$, with a median value of 8.6. Trends between metallicity and distance from the galaxy center are more clear in Figure 3.

Along B, gradients are symmetric around the 0 position up to 5″, then the south side shows a constant decline and a sudden increase at $r > 7''$, while the north side of the galaxy shows some fluctuations.

The minimum metallicity is $\log(\mathrm{O/H}) \sim 8.4$, while along A and B, for example, it is always $\geqslant$8.5. Finally, the E aperture catches one of the flattest gradients in the galaxy, with metallicity values >8.6 at all distances.

In Section 3.6.

Comparing the luminosity-weighted age and the ionization parameter (Figure 4), we find a clear anticorrelation.

In Section 4.2.4.

Figure 5 shows the distribution of the properties in the knots compared to those in the main body.

In Section 5.

P11695 has low levels of dust ($A_V < 1$ mag), a low ionization parameter value ($\log(q) \sim 6.8$), and a quite young luminosity weighted age ($\log(\mathrm{LWA}) \sim 8.4$).

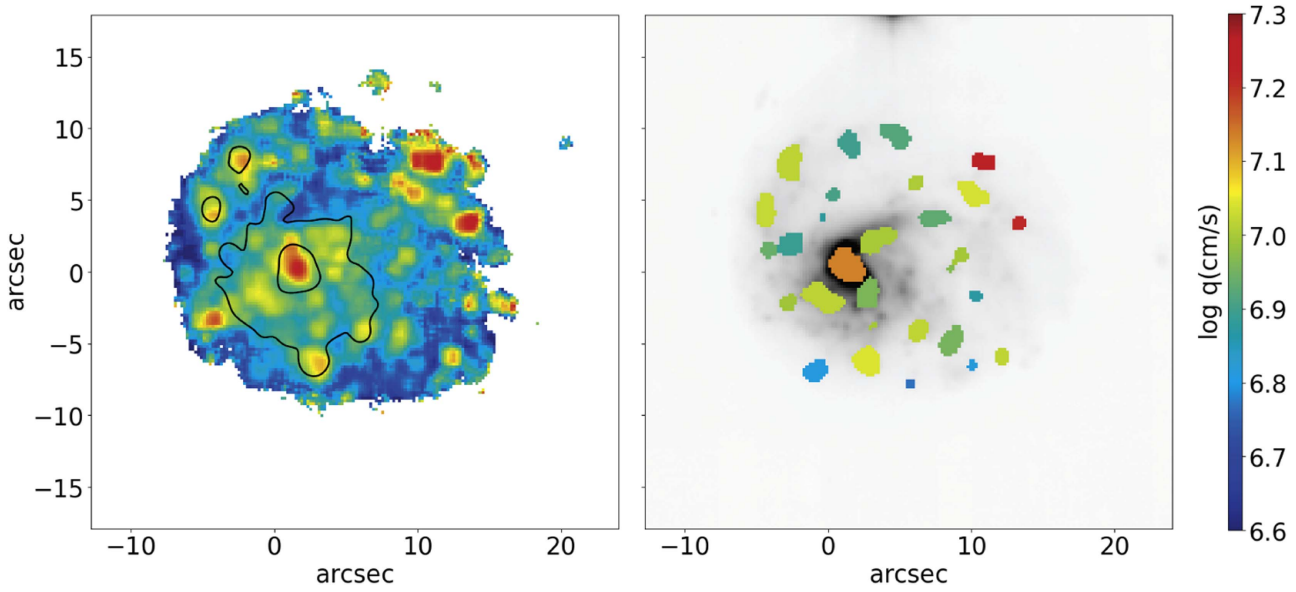

Figure 1. Ionization parameter (q) map. Left: contours represent the original body (see Figure 14 of Vulcani et al. 2018). Right: only regions corresponding to the 29 Hα knots identified in Figure 3 of Vulcani et al. (2018) are color coded according to the median q of each knots. In the background, the white-light image of the galaxy (Figure 2 of Vulcani et al. 2018) is shown, for reference.

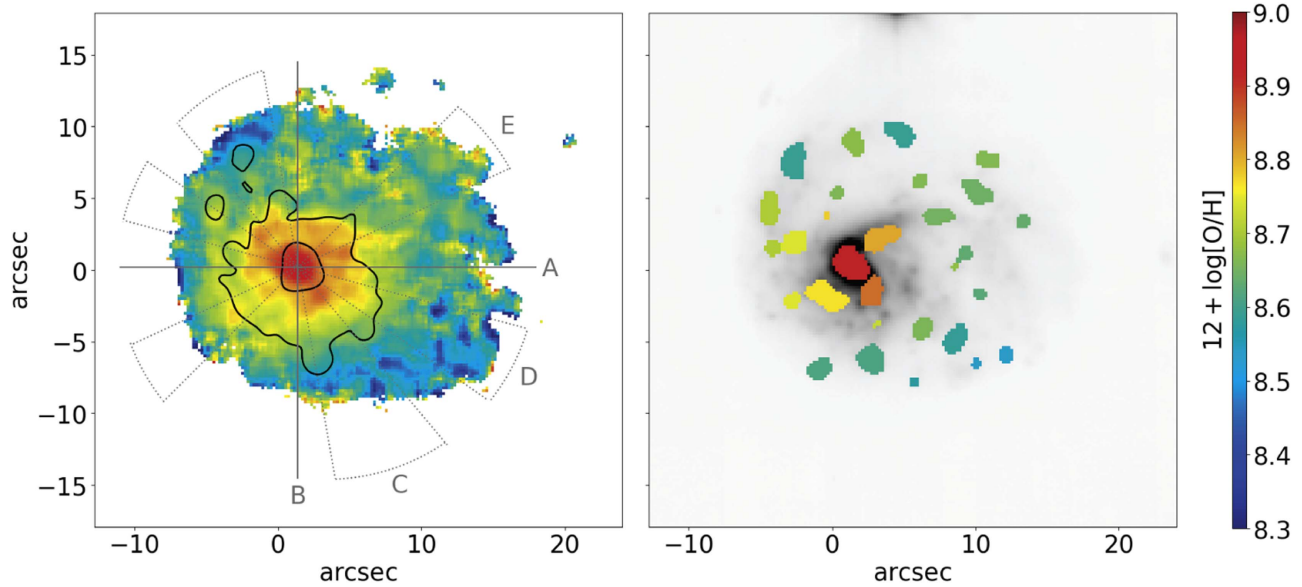

Figure 2. Gas metallicity map. Left: contours represent the original body (see Figure 14 of Vulcani et al. 2018). Slits (A, B) and conic apertures (C, D, E) used to extract metallicity gradients are also shown. Right: only regions corresponding to the 29 Hα knots identified in Figure 3 of Vulcani et al. (2018) are color coded according to the median metallicity of the knots. In the background, the white-light image of the galaxy (Figure 2 of Vulcani et al. 2018) is shown for reference.

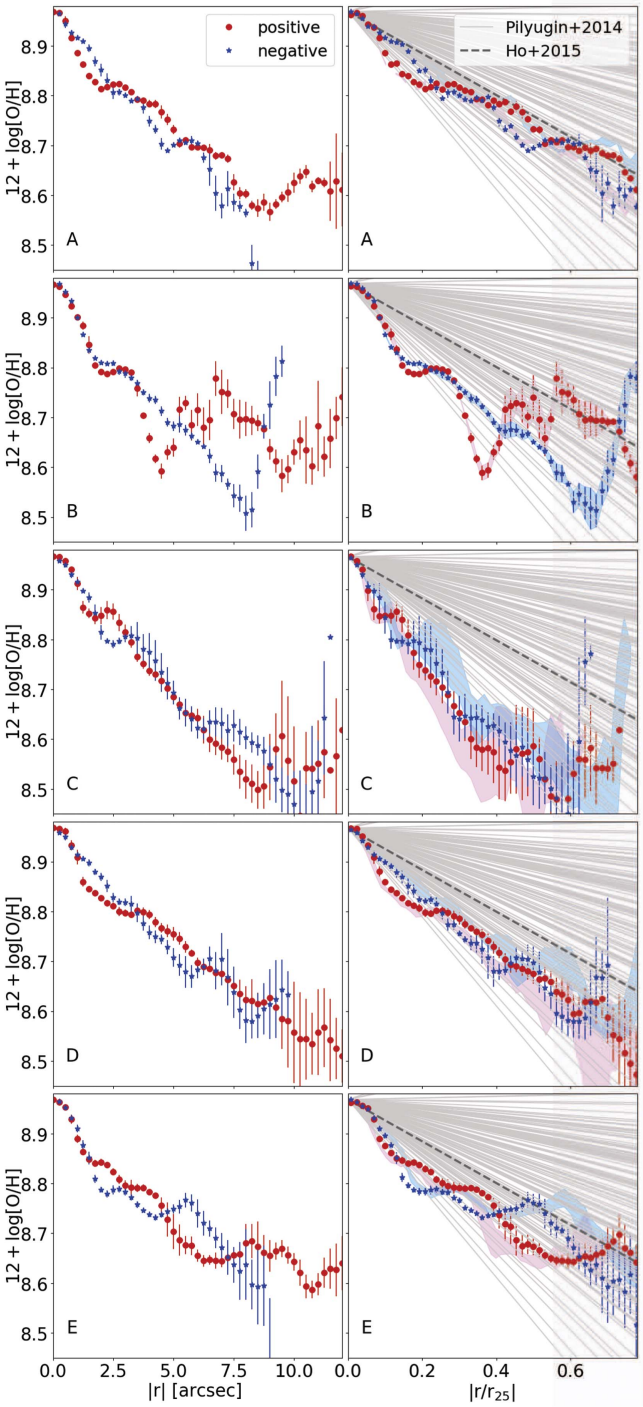

Figure 3. Gas metallicity gradients extracted along the directions (A, B, C, D, and E) shown in Figure 2. Errors represent the standard deviation (σ) computed using the values falling into the apertures. Red points correspond to the side of the slits north and/or west of the center (positive arcseconds), blue points correspond to the side of the slits south and/or east of the center (negative arcseconds). Left: profiles in arcseconds, not deprojected. Right: profiles normalized by a scale radius, all distances are deprojected considering the galaxy inclination and position angle. Shaded areas represent the profiles normalized adopting different scale lengths (see the text for details). Gray lines are from Pilyugin et al. (2014) and Ho et al. (2015).

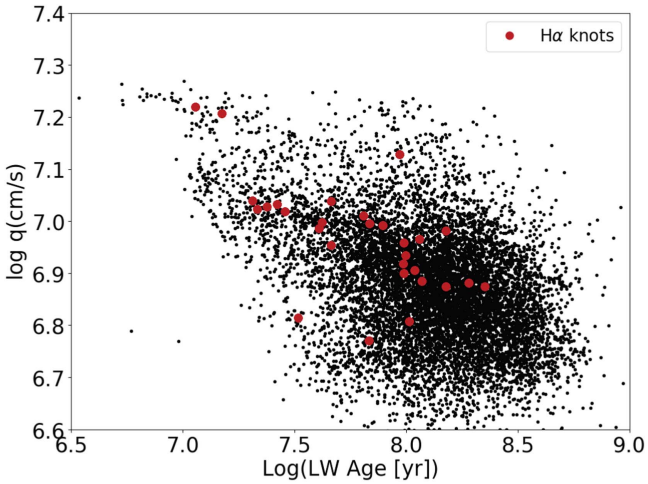

Figure 4. Correlation between the luminosity weighted age and the parameter of ionization. The average values computed in each Hα knot are shown with red circles.

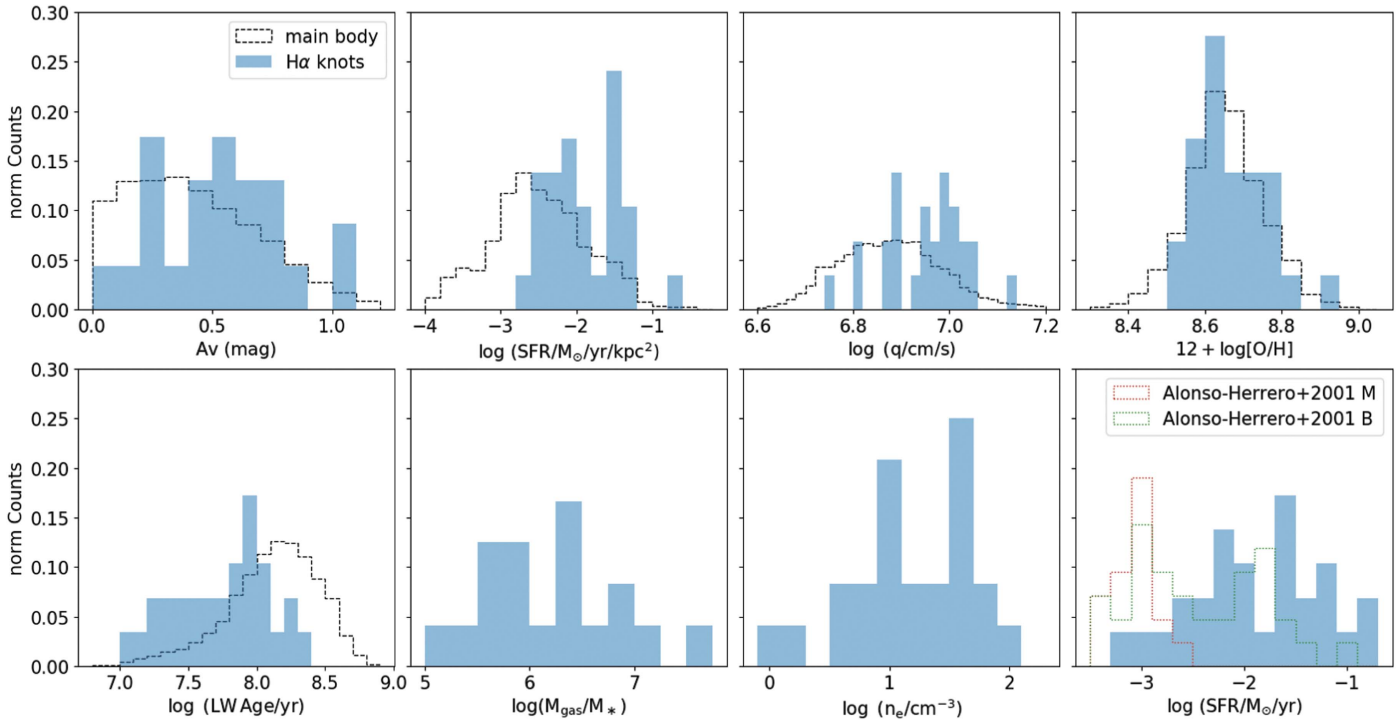

Figure 5. Normalized distribution of the properties of the Hα knots, compared to that of those of the galaxy main body (when meaningful). The A_V, SFR per unit kpc^2, parameter of ionization, metallicity, luminosity weighted age, gas mass, electron density, and SFR are shown. In the bottom right panel, we report for comparison the SFR distributions obtained from the Hα luminosity as measured by Alonso-Herrero & Knapen (2001) for H II regions in nearby galaxies. Estimates using only the brightest (B) and median (M) Hα luminosities are shown.

ORCID iDs

Benedetta Vulcani https://orcid.org/0000-0003-0980-1499
Bianca M. Poggianti https://orcid.org/0000-0001-8751-8360
Alessia Moretti https://orcid.org/0000-0002-1688-482X
Jacopo Fritz https://orcid.org/0000-0002-7042-1965
Daniela Bettoni https://orcid.org/0000-0002-4158-6496
Callum Bellhouse https://orcid.org/0000-0002-6179-8007

References

Alonso-Herrero, A., & Knapen, J. H. 2001, AJ, 122, 1350
Gullieuszik, M., Poggianti, B. M., Moretti, A., et al. 2017, ApJ, 846, 27
Ho, I.-T., Kudritzki, R.-P., Kewley, L. J., et al. 2015, MNRAS, 448, 2030
Pilyugin, L. S., Grebel, E. K., & Kniazev, A. Y. 2014, AJ, 147, 131
Poggianti, B. M., Moretti, A., Gullieuszik, M., et al. 2017, ApJ, 844, 48
Vulcani, B., Poggianti, B. M., Moretti, A., et al. 2018, ApJ, 852, 94